Journal of Power Sources 661 (2026) 238689

Contents lists available at ScienceDirect

Journal of Power Sources

journal homepage: www.elsevier.com/locate/jpowsour

Enhancing quasi solid-state dye-sensitized solar cell performance by encapsulating n-TiO_2 nanocrystallite-multi-layers by p-La_2O_3 charge separating layer

T.M.W.J. Bandara [a,*], R.D.M.A.C.B. Rajakarunarathne [a], R.P. Chandrika [a], L. Ajith De Silva [b], Kirthi Tennakone [c], G.R.A. Kumara [c], H.M.J.C. Pitawala [d], Prasad S. Wanninayake [e]

[a] Department of Physics and Postgraduate Institute of Science, University of Peradeniya, Peradeniya, Sri Lanka
[b] Department of Physics, University of West Georgia, USA
[c] National Institute of Fundamental Studies, Hanthana, Sri Lanka
[d] Faculty of Applied Sciences, Uva Wellassa University, Sri Lanka
[e] Department of Physics, University of Colombo, Sri Lanka

HIGHLIGHTS

- Investigated the effect of p-type La_2O_3 blocking layer on TiO_2 multilayer photoanodes.
- Efficiency significantly enhances with added La_2O_3 (327.32 nm) layer on 5th TiO_2 layer.
- The developed quasi-solid-state DSSC achieved a remarkable efficiency of 8.50 %.
- DFT + U study done for the 1st time explains the efficiency boost from added La_2O_3.
- 34 % efficiency gain with La_2O_3 confirms the value of adding layers such as p-La_2O_3.

GRAPHICAL ABSTRACT

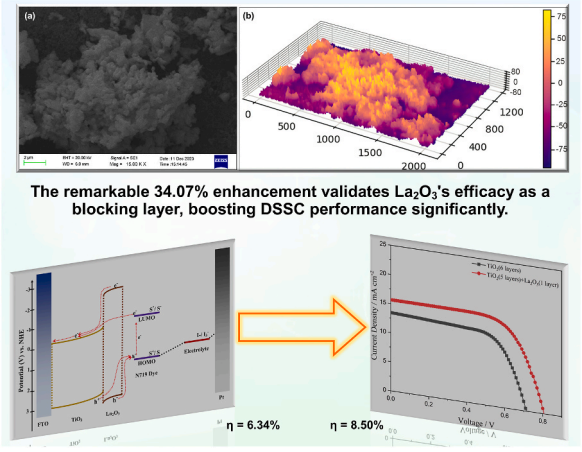

ARTICLE INFO

Keywords:
Dye-sensitized solar cells
Blocking layer
p-type La_2O_3
Photoanode
Electron transportation
Efficiency enhancement

ABSTRACT

This study presents a novel strategy to enhance the efficiency of dye-sensitized solar cells (DSSCs) by integrating a p-type La_2O_3 layer between the TiO_2 photoanode and the electrolyte. The p-La_2O_3 layer suppresses charge recombination by inhibiting electron transfer from TiO_2 to the electrolyte, improving charge separation and photovoltaic performance. Structural and compositional analyses (XRD, XRF, and SEM) confirm the presence of a uniform polycrystalline La_2O_3 layer on the 5-layered nanostructured TiO_2 electrodes. Mott-Schottky analysis confirms that TiO_2 is n-type and La_2O_3 is p-type, highlighting their complementary roles in efficient charge transfer. For the first time, DFT + U calculations were employed to investigate the band structure of La_2O_3. The

* Corresponding author.
E-mail addresses: awijendr@yahoo.com, wijendra@sci.pdn.ac.lk (T.M.W.J. Bandara).

https://doi.org/10.1016/j.jpowsour.2025.238689
Received 16 April 2025; Received in revised form 6 October 2025; Accepted 24 October 2025
Available online 29 October 2025

electron diffusion length was found to be enhanced upon the integration of p-La_2O_3, as revealed by electrochemical impedance analysis. The optimized device exhibits a power conversion efficiency of 8.50 %, with a short-circuit current density of 17.70 mA cm^{-2} and an open-circuit voltage of 0.73 V, representing a 34.07 % enhancement compared to the reference six-layer photoanode DSSC (6.34 %). The results demonstrate the effectiveness of a p-type La_2O_3 layer in boosting device performance by reducing charge recombination. To our knowledge, this is the first report demonstrating the effectiveness of La_2O_3 as a blocking layer in quasi-solid-state DSSCs, presenting one of the highest efficiencies.

1. Introduction

Photovoltaic systems are gaining popularity because solar energy is cleaner, inexhaustible, and more sustainable than traditional energy sources [1,2]. Over the last decade, dye-sensitized solar cells (DSSCs) have emerged as a promising alternative to conventional photovoltaic technologies due to their low fabrication cost, simple manufacturing procedures, efficiencies comparable to those of non-crystalline silicon solar cells, good performance under poor or diffuse lighting, and adaptability to various sensitizers [3–5]. A typical DSSC consists of a dye-sensitized mesoporous semiconductor photoanode (commonly TiO_2) deposited on a transparent conducting oxide substrate, a liquid/gel electrolyte containing a redox couple (often iodine/iodide), and a counter electrode, frequently coated with platinum [6–8]. Additionally, different n-type and p-type metal oxide semiconductors (e.g., TiO_2, ZnO, SnO_2, WO_3, NiO, $CuCrO_2$) are also employed in the fabrication of DSSCs [9–14]. Anatase-phase TiO_2 stands out due to its favorable bandgap (~3.2 eV), excellent chemical stability [15,16], and ideally positioned conduction band edge just below the lowest unoccupied molecular orbital (LUMO) of commonly used dyes such as N719 [17]. This alignment is crucial for effective electron injection and transport, thereby enhancing the overall performance of DSSCs.

It is the larger surface area of nanoporous TiO_2 that's responsible for providing effective dye adsorption; this characteristic, in turn, enhances light harvesting and boosts photocurrent generation [18]. Despite these advantages, a significant challenge remains: the recombination of photogenerated electrons with either oxidized dye molecules or redox species in the electrolyte, especially at the TiO_2/electrolyte interface which needs to be minimized. Such charge recombination processes substantially limit the attainable solar-to-electricity conversion efficiency and the stability of DSSCs. Surface modifications of the TiO_2 photoanode with blocking layers or charge-separating layers have gained considerable attention. These layers act as barriers to electron recombination by inhibiting back-electron transfer to the electrolyte while improving electron injection efficiency from the dye. Materials such as $BaCO_3$, Al_2O_3, MgO as well as wide bandgap semiconductors with higher conduction band edges (ZrO_2, In_2O_3, Nb_2O_5, ZnO) [19] have demonstrated varying degrees of success in enhancing device performance by suppressing interfacial recombination and improving charge transport kinetics [20].

In addition to optimizing the photoanode material, recent advancements in DSSCs have moved beyond classical dyes to explore sustainable and high-performing alternatives. Natural dyes (*Ligustrum vulgare*, *Juniperus sabina*, *Papaver rhoeas*, *Hyoscyamus reticulatus*, *Mahonia aquifolium,* and *Hedera helix* fruits [21–23]) offer eco-friendly, low-cost options, although the efficiencies remain limited. Synthetic approaches, such as AZO-based dyes (0.47 % PCE) [24] and D-π-A-π-A metal-free structures (QX-TPA: 6.80 % PCE) [25], have demonstrated improvements in charge transfer through molecular design. In view of the above, dye optimization and surface modification of the photoanode can significantly improve the efficiency of DSSCs.

Although this work focuses on investigating La_2O_3 as a novel p-type blocking layer, it is worthwhile to examine the previous investigations of the effects of other p-type blocking layers on DSSC the performance. The most recent research on DSSCs with various p-type blocking layers is presented in Table 1. Compared to previous studies, the present work exhibits significantly higher performance. While $CuCrO_2$ nanoparticles have shown relatively higher values in earlier work, the efficiencies reported in this study exceed those by more than an order of magnitude, thus highlighting the importance of the present study.

In this study, we present a novel approach to enhance the performance of DSSCs. This method involves introducing an ultra-thin p-type La_2O_3 charge-separating film at the interface between TiO_2 and the electrolyte for the first time. The primary objective is to mitigate charge recombination rates by suppressing electron transfer from TiO_2 to the electrolyte. In this context, La_2O_3 is used as a promising candidate for interface engineering in DSSCs due to its unique physicochemical properties: a high dielectric constant, excellent thermodynamic stability, and notably, an elevated conduction band edge relative to TiO_2. These attributes suggest that ultra-thin La_2O_3 layers deposited on TiO_2 photoanodes can create an effective energy barrier that minimizes electron back-transfer to the electrolyte without hindering electron injection from the dye. La_2O_3 possesses a high dielectric constant and a conduction band edge positioned higher than that of TiO_2 [32]. The energy barrier created by this band alignment inhibits electron leakage while still permitting efficient electron injection from the dye into TiO_2. This optimal band offset improves charge separation and transport. The thermodynamic stability of La_2O_3 under operating conditions ensures the durability and long-term functionality of the blocking layer, thereby enhancing device stability.

Furthermore, the ultra-thin La_2O_3 interlayer modifies interfacial electron transfer kinetics by acting as a charge-separating layer, which improves electron diffusion length and reduces recombination resistance, as evidenced by electrochemical impedance spectroscopy [33]. By strategically introducing ultra-thin La_2O_3 films, charge recombination is effectively minimized, resulting in an enhanced overall efficiency of DSSCs. This study highlights the critical role of La_2O_3 in altering electron transfer dynamics within the DSSC architecture, providing valuable insights into its potential as a blocking layer to optimize electron transport and enhance photovoltaic performance.

By regulating charge transport and recombination processes, surface modifications with blocking layers play a crucial role in enhancing the performance of various electronic devices. When strategically introduced at interfaces, these layers mitigate electron recombination, thereby enhancing efficiency and functionality in electronic applications [34]. In one study, a nanoporous TiO_2 electrode was modified with $BaCO_3$ for quasi-solid-state DSSCs. The $BaCO_3$ modification enhances dye adsorption by leveraging its higher surface basicity compared to TiO_2. The resulting increase in conversion efficiency from 5.53 % to 6.96 %, a 25.9 % improvement under 30 mW cm^{-2}, indicated that $BaCO_3$ induces a negative shift in the TiO_2 conduction band, leading to

Table 1
Performance comparison of different p-type blocking layer-based DSSCs.

Photoanode	J_{SC}/mA cm^{-2}	V_{OC}/V	*ff*	*PCE*/%	Reference
$CuCrO_2$ + Zn	0.54	0.28	0.42	0.075	[14]
NiO-Ac	1.45	0.08	0.36	0.042	[13]
NiO	3.05	0.17	0.33	0.164	[26]
$CuGaO_2$ nano plates	2.05	0.20	0.45	0.182	[27]
$CuCrO_2$ nanoparticles	1.23	0.73	0.48	0.530	[28]
$CuCrO_2$ + Mg	1.51	0.20	0.45	0.132	[29]
LaOCuS nanoparticles	0.04	0.15	0.26	0.002	[30]
Cu_2O	1.30	0.71	0.46	0.420	[31]

enhanced DSSC performance [35]. In the study [20], a semiconductor TiO_2 photoanode was fabricated with an insulating layer of Al_2O_3 to augment the performance of DSSCs. The DSSC featuring the developed photoanode achieved a maximum efficiency of 4.04 %, marking a noteworthy enhancement of 15.5 % [36]. Similarly, the PCE of DSSC was further improved by adding an MgO blocking layer to the TiO_2 photoanode. The optimized thickness of the MgO layer resulted in the highest conversion efficiency of 5.12 %, along with a notable J_{SC} of 18.15 mA cm^{-2} and a V_{OC} of 0.571 V [5].

Surface modifications involving higher conduction band edge semiconductor layers represent a crucial strategy in improving the performance of electronic devices. By introducing semiconductors with elevated conduction band edges, these modifications aim to enhance charge transport and reduce recombination, contributing to the overall efficiency and functionality of electronic applications [37]. In related studies, the DSSC's TiO_2 photoanode was developed using ZrO_2, which resulted in an efficiency gain due to ZrO_2's larger conduction band edge. The optimized configuration achieved a maximum efficiency of 6.97 % [38]. In a separate study, the photoanode was constructed using In_2O_3 with varying numbers of layers, and single coatings of In_2O_3 on the TiO_2 working electrode demonstrated an efficiency increase from 3.6 % to 4.9 %. Notably, thinner coatings exhibited the highest efficiency of solar cells [39]. In another study, DSSC devices were assembled with a photoanode configuration comprising Nb_2O_5/TiO_2 bilayer and TiO_2 multilayers, utilizing N719 dye, iodide-based electrolytes, and a platinum counter electrode. The highest efficiency of 5.4 % was attained in the bilayer photoanode system, with an optimal thickness of Nb_2O_5 [40].

The use of solvents made from volatile organic compounds as a medium of transport for redox species in DSSCs presents sealing, safety, and leakage challenges and limits the flexibility of device construction and development as viable outdoor and indoor applications [41,42]. Polymer gel electrolytes are an alternative to problematic liquid electrolytes in DSSCs; however, the efficiency of high-quality solid-state devices suffers due to the lower conductivity of gel electrolytes compared to liquid electrolytes. Importantly, in the present study, volatile solvent-based electrolytes were not used. Instead, a gel polymer electrolyte was utilized to achieve high stability [43,44]. The cell stability and efficiency exhibited are a result of selected gel polymer electrolytes. In particular, the efficiency is improved using the ionic liquid 1-hexyl-3-methylimidazolium iodide (HMII), 4-tert-butylpyridine (4TBP), and combinations of mixed salts and solvents [45,46].

This study represents a significant advancement in the field of DSSCs by introducing an ultra-thin p-type La_2O_3 charge-separating/blocking layer between the n-type TiO_2 photoanode and the electrolyte in a quasi-solid-state DSSC configuration, which has not been previously reported. The strategic integration of La_2O_3 addresses a critical limitation in DSSC performance: interfacial charge recombination. This recombination negatively impacts charge separation efficiency and lowers the overall photovoltaic output. By suppressing undesirable electron back-transfer to the electrolyte, the La_2O_3 layer enhances charge carrier lifetime and transport. As a result, devices incorporating this layer show higher power conversion efficiency compared to conventional cells. This work provides valuable insights into interface engineering strategies and material incorporation for quasi-solid-state DSSCs, paving the way toward more efficient, stable, and practical photovoltaic devices. The demonstrated approach has the potential to be broadly applied or adapted in other photoelectrochemical systems to mitigate charge recombination losses, thereby advancing renewable energy technologies.

2. Experimental

2.1. Materials

The study employed conducting substrates composed of fluorine-doped tin oxide (FTO), which had a sheet resistance of 10 Ω/sq. Moreover, titanium dioxide (TiO_2) nano powders, namely P25 (with an average particle size of 21 nm) and P90 (with an average particle size of 13 nm), were obtained from Evonik Germany for the study. The high-purity (99 %) lanthanum oxide (La_2O_3) powder utilized in this study was directly procured from BDH Chemical Ltd., England. Solaronix SA supplied the ruthenizer 535-bisTBA (N719) dye that was used to sensitize these electrodes. Aldrich provided polyethylene oxide (PEO) (MW - 4,000,000), polyethylene glycol (PEG) (MW - 4000), iodine (I_2), ethylene carbonate (EC), propylene carbonate (PC), LiI, tetrahexylammonium iodide (Hex_4NI), 1-hexyl-3-methylimidazolium iodide (HMII), and 4-tert-butylpyridine (4TBP), all of which had purities exceeding 98 %. Before use, PEO, Hex_4NI, and LiI were vacuum-dried at 50 °C for ~2 h.

2.2. Preparation of the TiO_2/La_2O_3 photoanodes

In this study, an improved photoelectrode for DSSCs was created by employing five layers of TiO_2 nanoparticles that had been initially optimized in a pilot study [47,48]. Fig. 1(a) displays the configuration of the improved electrode.

To prepare the first layer, 0.5 g of TiO_2 nanoparticles with an average size of ~13 nm (P90 powder, as specified by the manufacturer) was ground with 2 ml of 0.1 M HNO_3 in an agate mortar for approximately 30 min to obtain a well-dispersed TiO_2 slurry. The dispersion of TiO_2 nanoparticles was spin-coated over a pre-cleaned FTO substrate measuring 1 cm × 2 cm at a rate of 2300 rpm for around 2 min. Before spin coating, Scotch tape was used to cover half of the FTO plate to prevent the TiO_2 coating from accessing the electrical connections. After air-drying for around 12 h, the first layer was sintered in air at 450 °C for 30 min.

A similar process was used to prepare succeeding layers, but with different spin coating rates and particular slurry compositions. The second layer was generated with a spin coating rate of 1000 rpm. In the third layer, a slurry was created by grinding 0.5 g of nanoparticles with an average size of ~21 nm (P25 TiO_2 powder) and 2 ml of 0.1 M HNO_3 in an agate mortar. Add 0.1 g of 4000 molecular weight PEG and a few drops of Triton X 100 (surfactant) to the slurry and thoroughly mix it. The slurry that formed was spin-coated at 1000 rpm for 2 min before being sintered at 450 °C. The fourth and fifth layers have been produced by repeating the procedure used for the third layer.

The sixth layer required the creation of a slurry by grinding 0.5 g of La_2O_3 powder and 2 ml of 0.1 M HNO_3 in an agate mortar to obtain a well-dispersed TiO_2 slurry. Add 0.1 g of 4000 molecular weight PEG and a few drops of Triton X 100 (surfactant) to this slurry and stir thoroughly. The resulting slurry was deposited onto the substrate via spin coating at 1000 rpm for 2 min and then dried in ambient air for 12 h before being sintered at 450 °C [49,51]. All spin-coating procedures were carried out at room temperature (25 ± 2 °C) at controlled relative humidity (65 ± 5 %). A fixed spin-coating acceleration rate of 500 rpm/s was applied to all samples for uniform film deposition. The technique produced photoelectrodes with six layers of TiO_2/La_2O_3 nanoparticles, as shown in Fig. 1(a).

The resulting photoelectrodes are heated to roughly 100 °C and immersed in a warmed solution (about 60 °C) containing 0.3 mM N719 dye dissolved in 100 % ethanol. The electrode soaked in the dye solution was left to cool down to room temperature. Following about 24 h of immersion, the electrodes were carefully removed from the dye solution and rinsed with ethanol to remove any partially bound surplus dye.

2.3. Preparation of the GPE

The gel polymer electrolyte (GPE) has been generated using the stoichiometric composition of $PEO_{(10)}EC_{(40)}PC_{(40)}Hex_4NI_{(0.8)}LiI_{(1.2)}I_{2\,(0.2)}$, following prior studies [50,51]. Table 2 shows the amounts utilized for the GPE. To prepare the GPE series, a mixture of EC and PC co-solvents was first dissolved in a sealed glass container. Later, 4TBP

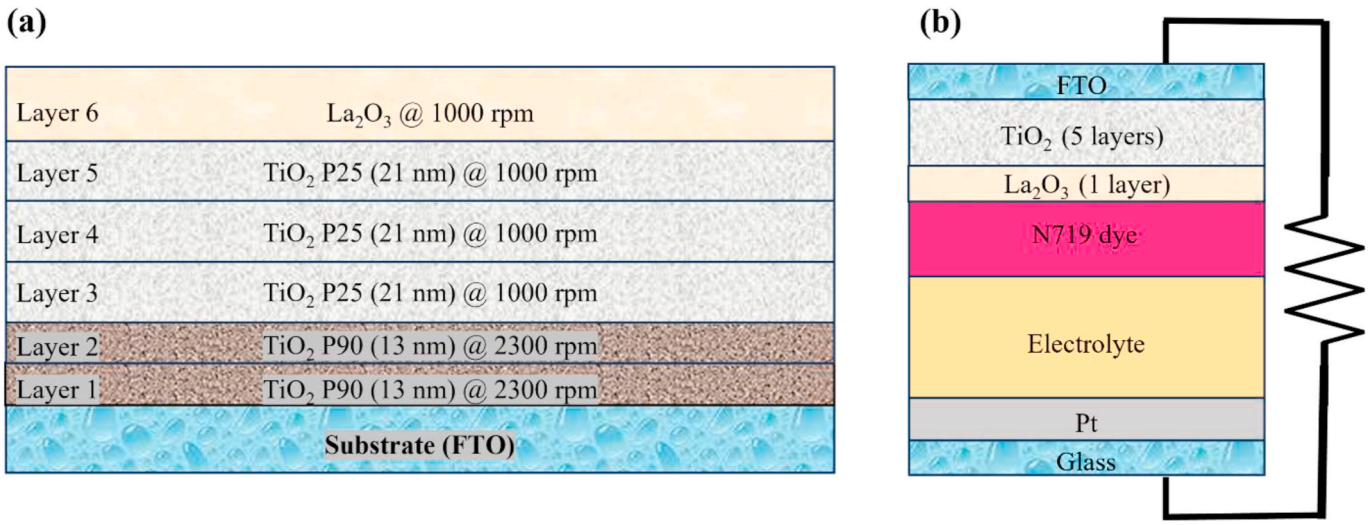

Fig. 1. (a) Schematic representation (not to scale) of the photoanode design with five layers of TiO_2 nanoparticles and one layer of La_2O_3, (b) The configuration of DSSCs.

Table 2
Mass fractions and molar ratios of PEO-based gel polymer electrolyte.

Component	Weight/mg	Molar ratio
EC	400.00	40.00
PC	463.50	40.00
HMII	7.55	0.25
4TBP	13.05	0.85
LiI	18.25	1.20
Hex_4NI	43.75	0.80
I_2	5.75	0.20
PEO	50.00	10.00

and HMII were added to the mixture. Upon that, needed amounts of Hex_4NI and LiI were added, and the mixture was agitated. PEO was then mixed into the salt solution and vigorously agitated to ensure homogeneity. The mixture was subsequently heated to approximately 100 °C while being constantly mixed until it formed a clear slurry. Once the mixture had dropped to 40 °C, 12 mg of I_2 was added to the slurry and stirred constantly.

2.4. Fabrication of DSSCs

The GPE was placed separately between a platinum (Pt) counter electrode and a TiO_2/La_2O_3 photoelectrode sensitized with N719 dye. This layout was utilized to produce a series of DSSCs. Fig. 1(b) depicts the structural configuration of the DSSC set, identified as glass/FTO/TiO_2/N719/electrolyte/Pt/glass.

2.5. Characterization of the photoanode

The characterization of the prepared photoanode in this study involved multiple analytical techniques. X-ray diffraction (XRD) analysis was performed using a RIGAKU Ultima IV X-ray diffractometer, which utilizes Cu Kα radiation with λ = 1.54184 Å to investigate the crystalline structure. X-ray fluorescence (XRF) analysis was performed using the HELMUT FISCHER GMBH + CO KG X-ray HAN to verify the availability and composition of the La_2O_3 film. Morphological details were examined through scanning electron microscopy (SEM) using the Zeiss Evo LS15 SEM instrument. Additionally, the Mott-Schottky characterization was performed on the photoanode at a frequency of 2000 Hz to identify the semiconductor type and the flat-band potential values of the photoanode layer. The measurements were taken utilizing a Metrohm Autolab impedance analyzer (PGSTAT 128N, Netherlands). Furthermore, UV–vis spectrophotometry, using the SHIMADZU UV-1900i UV–Vis Spectrophotometer, complemented the comprehensive material characterizations.

First-principles calculations based on Density Functional Theory (DFT) were conducted to study the bulk structures of TiO_2 and La_2O_3. Their heterostructure was modeled using a slab with a vacuum layer (20 Å) to prevent interactions between periodic images. The computations were carried out using the Quantum ESPRESSO package with Projector Augmented-Wave pseudopotentials. The Generalized Gradient Approximation (GGA) with the Perdew-Burke-Ernzerhof (PBE) functional was employed. To correct for the typical DFT underestimation of band gaps, the DFT + U method was applied. This approach incorporated on-site Coulomb interactions to improve accuracy.

2.6. Characterization of DSSCs

The PEC-LO1 solar simulator was used to assess the current-voltage (*I-V*) properties of the manufactured solar cells under 1000 W m^{-2} (AM1.5) irradiation. The cell's active area was 0.19 cm^{-2}, with a theoretical scan rate of 0.01 V s^{-1}. *I-V* measurements were obtained for ~3 h (at 10-min intervals) under continuous irradiation.

Under specific experimental conditions, the electrochemical impedance spectra (EIS) of the solar cells were measured with a bias equivalent to the open-circuit voltage (V_{OC}). These observations were made over a frequency range of 1 Hz–10^6 Hz, with the alternating current (AC) amplitude set at 10 mV. The evaluations were done with the solar cell within a Faraday cage, which ensured that it was isolated from any other electromagnetic frequencies. The findings were subsequently recorded through the Metrohm Autolab impedance analyzer (PGSTAT 128N, Netherlands).

3. Results and discussion

3.1. Surface morphology of the photoanode

SEM imaging is a tool for the comprehensive characterization of the photoanode's morphology, enabling detailed examination of surface features and particle distributions. Fig. 2-(A) provides electron microscope (SEM) images that depict the morphological characteristics of the engineered photoanode. SEM images of the first and second layers showed similar morphology, which can be a result of identical film preparation methods and ingredients used; thus, an SEM image of the first layer is shown in Fig. 2-(A) (a). SEM images of 3–5 layers of TiO_2,

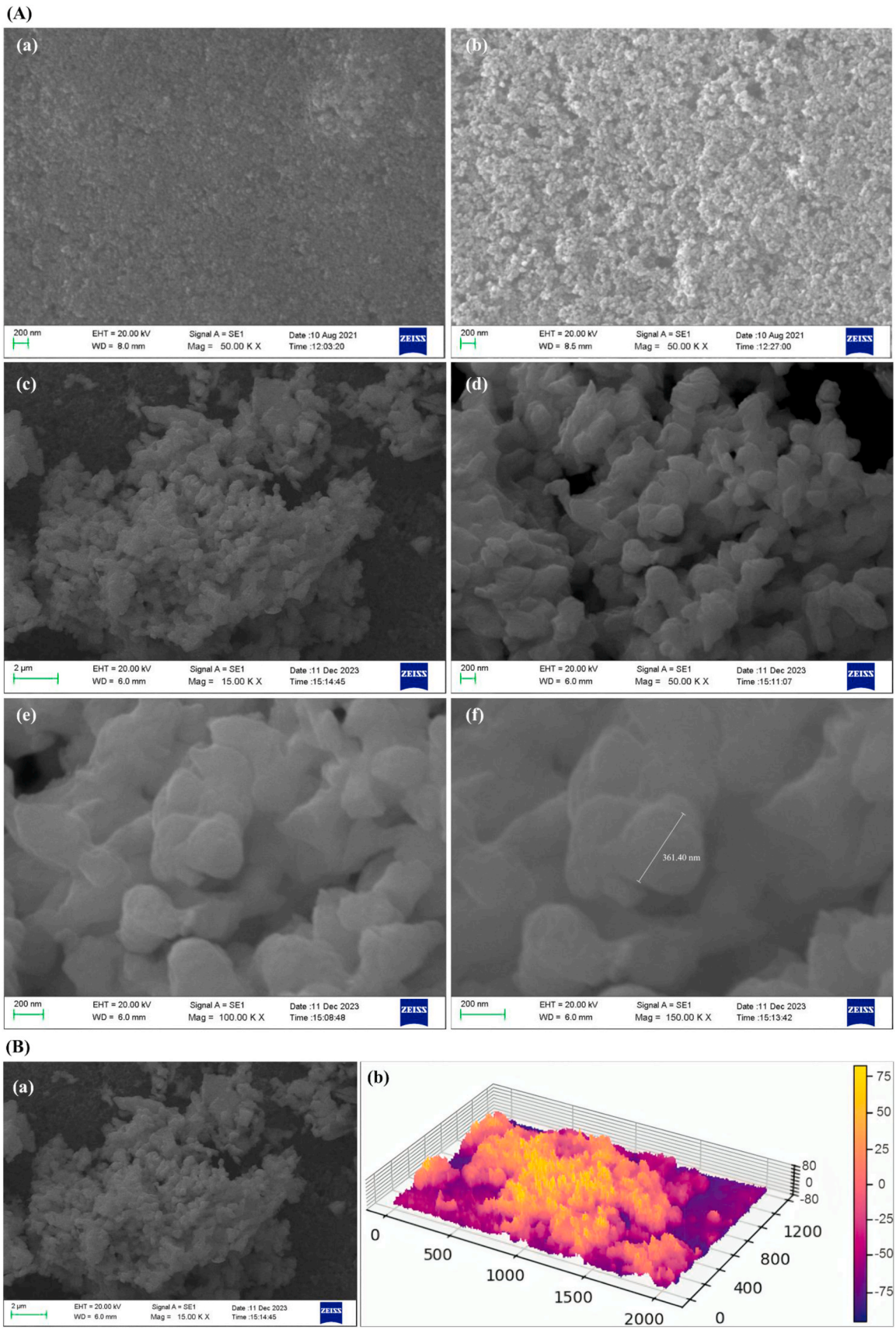

Fig. 2. (A) - SEM images of (a) the first TiO_2 layer (P90, 13 nm), (b) the third TiO_2 layer (P25, 21 nm) with the magnification of × 50.00K, and (c–f) the La_2O_3 top layer at varying magnifications (× 15.00K to × 150.00K)/(Scale bars: (a–b) 200 nm, (c) 2 µm, (d–f) 200 nm). (B)–(a) SEM image of the La_2O_3 layer (× 15.00K); (b) 3D grayscale thickness map derived from SEM image analysis to measure the average thickness (average thickness: 1.43 ± 0.13 µm).

which were prepared using a particle size of 21 nm, exhibited a similar morphology, and thus an image of a 3-layer electrode is shown in Fig. 2-(A) (b). Notably, the SEM images showcased a discernible top layer composed of La_2O_3, which was strategically implemented as a blocking layer within the photoanode architecture. Through meticulous observation and analysis of the images presented in Fig. 2-(A) (c)–(f), it becomes evident that the La_2O_3 nanoparticles are evenly spread across the surface of the TiO_2 layer, and they are interconnected. The SEM confirmed that La_2O_3 was successfully formed within the photoanode structure, validating the effectiveness of the surface modification process. The highly porous structure of La_2O_3 is also evident from the SEM images. Furthermore, the SEM images enabled quantitative analysis of the La_2O_3 particle size distribution, which is a key parameter affecting the photoanode's performance characteristics. The average particle size of the La_2O_3 nanoparticles is 327.32 nm, as measured by image analysis using ImageJ software.

Furthermore, a detailed investigation into the structure involved processing the grayscale 3D image maps programmatically. The average thickness of the deposited La_2O_3 layer was calculated using SEM images from Fig. 2-(A) (c), as shown in Fig. 2-(B) (b). The calculations performed on the 3D mapping image yielded a precise thickness measurement of 1.43 ± 0.13 μm. In this method, the image was analyzed using the Python platform. The analysis process involved: (1) spatial calibration to the SEM scale bar (nm/pixel resolution), (2) grayscale intensity

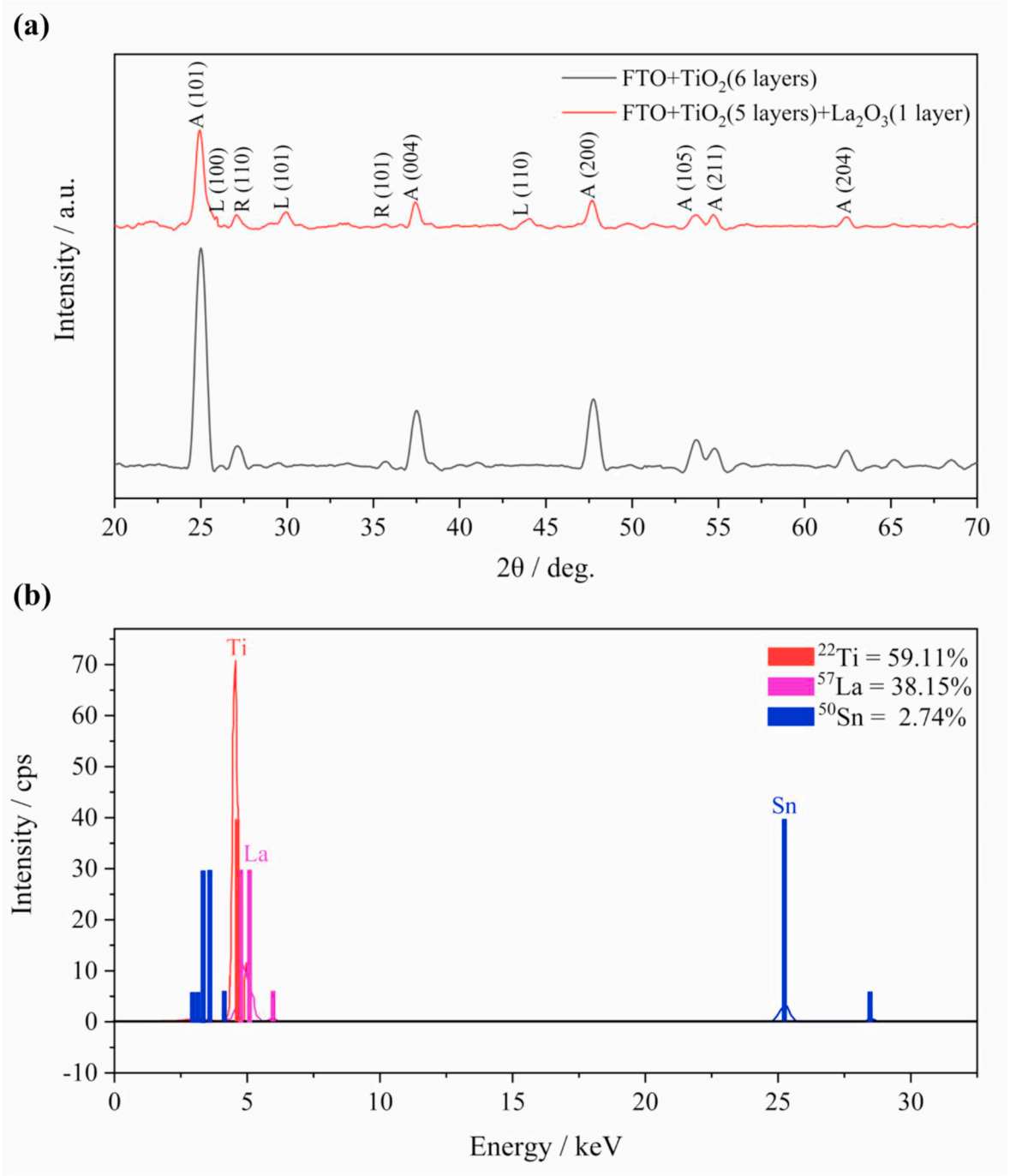

Fig. 3. (a) - XRD patterns of the control (bare TiO_2 photoanode) and the developed photoanode; TiO_2 (A), anatase; TiO_2 (R), rutile; La_2O_3 (L), cubic phase/(b) - XRF analysis of the photoanode developed by depositing La_2O_3 on a 5-layer TiO_2 electrode.

thresholding (Otsu's Approach-Python OpenCV) to extract La_2O_3 from the TiO_2 substrate, and (3) 3D surface reconstruction from intensity gradients. The reproducibility of the measurement was confirmed by repeated analyses using samples with different orientations (<10 % deviation). This non-destructive approach provides detailed information on the surface and dimensional characteristics of the developed photoanode, with the use of SEM enhancing the understanding of its structural properties.

3.2. Structural and compositional properties of the photoanode

The crystalline structure and cryptography of the control (bare TiO_2 photoanode) and the modified photoanodes were systematically investigated through X-ray diffraction (XRD) analysis, as depicted in Fig. 3-(A). The XRD spectra revealed characteristic anatase (A) peaks at 2θ values of 24.99°, 37.45°, and 47.72°, which were consistently observed in both the control and developed photoanodes. Distinctive changes were evident in the XRD spectra of the modified photoanodes by adding La_2O_3, remarkably exhibited in the presence of additional diffraction peaks. Notably, three discernible peaks at approximately 2θ values of 25.00°, 29.85°, and 37.45° were identified, corresponding to the cubic (C) La_2O_3 phase, as confirmed by the Joint Committee on Powder Diffraction Standards (JCPDS) reference code 22–369 [52]. This observation signifies the successful incorporation of La_2O_3 into the multi-layer photoanode structure.

The identification of these specific crystalline phases is crucial, as it provides insights into the structural modifications. The *d*-spacing, crystallite size, lattice strain, and dislocation density related to the significant peaks in Fig. 3-(A) were determined using the Debye-Scherrer relations, as given in the equations.

$$D = \frac{0.94\lambda}{W \cos\theta} \tag{1}$$

$$\varepsilon = \frac{W \cos\theta}{4} \tag{2}$$

$$\delta = \frac{1}{D^2} \tag{3}$$

where, D is the crystallite size, λ is the X-ray wavelength, θ is Bragg's angle, and w is the full width at half maximum (FWHM) of the peak in radians. The lattice strain, ε, and the dislocation density, δ, were calculated using equations (2) and (3). The calculated parameters are given in Table 3. These analytical results of crystallite size (10–170 nm) and lattice strain (2.1-3.6 × 10^{-3}) values were compared with the literature values for polycrystalline oxides of Al-Cu co-doped ZnO thin films and AZO nanostructures [53,54], particularly in their strain behavior at material interfaces.

The presence of both anatase and cubic La_2O_3 phases in the modified photoanodes suggests a synergistic crystalline structure. Notably, the average particle size from SEM measurement (327.32 nm, Fig. 2) is greater than the crystallite sizes obtained from XRD estimation (10–170 nm, Table 3). This is because SEM only captures the physical agglomeration of particles, whereas XRD estimates the size of isolated crystalline domains based on interpreting the broadening of diffraction peaks. The greater particle size estimated using SEM indicates that the grains observed consist of multiple small crystallites, typical of a polycrystalline microstructure.

X-ray fluorescence (XRF) analysis was systematically conducted on the developed photoanode, and the results are depicted in Fig. 3-(B). This analytical approach enabled a comprehensive examination of the elemental composition and their respective concentrations within the photoanode. The instrument's penetration depth, ~10 μm, ensured thorough data acquisition, capturing information from the entire thickness of the photoanode, which measures ~5.7 μm. The elemental composition of the photoanode, elucidated by XRF, revealed a predominant presence of titanium (Ti) at 59.11 %. This prevalence is attributed to the deposition of 5 layers of TiO_2 in the photoanode structure.

Additionally, lanthanum (La) was identified as the second most abundant element, constituting 38.15 % of the photoanode composition (elemental weight percentages of the photoanode). The oxygen content cannot be determined from XRF analysis; however, based on XRD analysis, the presence of TiO_2 and La_2O_3 was confirmed. Tin (Sn) was detected in the sample, originating from the fluorine-doped tin oxide (FTO) substrate. It makes a discernible contribution to the overall elemental composition. Additionally, based on XRF and XRD analysis, the molar percentages of TiO_2, La_2O_3, and SnO_2 were calculated to be 88.50 %, 9.85 %, and 1.65 %, respectively, for the photoanode.

Overall, the XRF analysis provides definitive evidence of the presence of La_2O_3 on the photoanode. The elemental composition assessment through XRF confirms the successful incorporation of La_2O_3 into the photoanode structure. This verification serves as a crucial validation of the intentional modification, attesting to the accurate and specific characterization of the developed photoanode.

3.3. Optical properties of the photoanode

The UV–Vis absorption spectrum was obtained for photoanodes with a single layer deposition on FTO substrates using TiO_2 P90, TiO_2 P25, and La_2O_3. The analysis focused on verifying the absorption wavelength regions of each photoanode and determining the band gap energies of the respective materials using Tauc plot analysis, as represented in Fig. 4 (a). The Tauc plot for indirect transitions is a graphical representation of $(\alpha h\nu)^2$ [2] vs. photon energy $(h\nu)$, where α is the absorption coefficient, h is Planck's constant, and ν is the frequency of light. This plot is employed to extrapolate the bandgap energy of a material by identifying the intersection point where the linear component of the plot intersects the energy axis. The equation related to the Tauc plot calculations is

Table 3
XRD peak data analysis results of the photoanode. Calculated values of the 2θ, crystal plane, *d* spacing, average crystallite size (*D*), strain (ε), and dislocation density (δ) for two photoanodes.

Photoanode	2θ (deg.)	Crystal plane	*d* spacing	FWHM (deg.)	Average CrystalliteSize, *D* (nm)	Average Strain, ε (× 10^{-3})	Average Dislocation density, δ (× 10^{-3} nm^{-2})
TiO_2	24.99	A(101)	3.5597	0.60	14.16	2.56	4.98
	37.45	A(004)	2.3996	0.56	15.64	2.31	4.09
	47.72	A(200)	1.9043	0.62	14.63	2.47	4.67
	53.69	A(105)	1.7057	0.70	13.86	2.61	5.21
	54.70	A(211)	1.6767	0.85	10.94	3.31	8.35
	62.40	A(204)	1.4871	0.60	15.57	2.33	4.13
	27.11	R(110)	3.2872	0.56	15.24	2.38	4.30
	35.77	R(101)	2.5090	0.77	11.32	3.20	7.80
La_2O_3	24.93	L(100)	3.5680	0.05	169.95	0.21	0.03
	29.85	L(101)	2.9910	0.71	12.09	2.99	6.84
	44.07	L(110)	2.0530	0.89	10.06	3.60	9.89

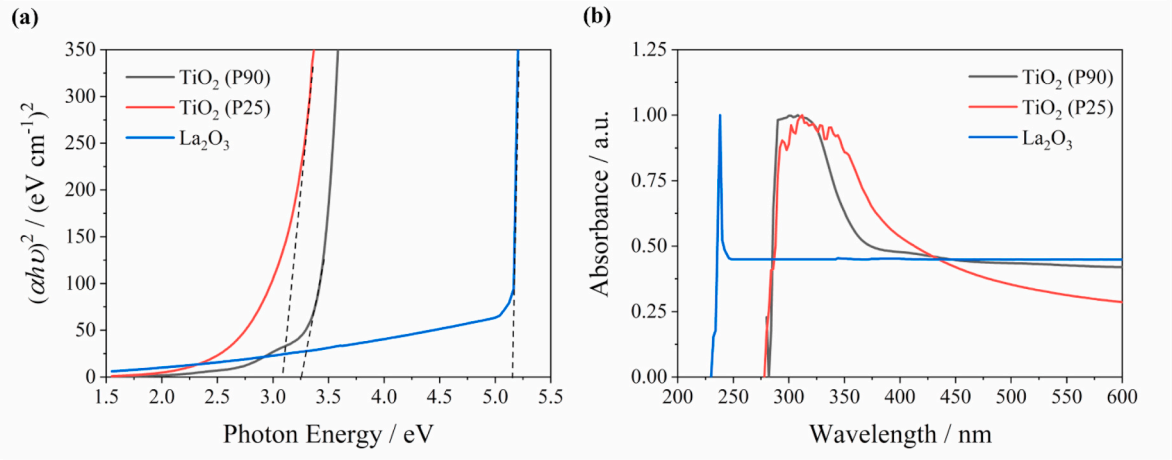

Fig. 4. (a) Tauc plot, (b) UV–Vis spectra for the TiO_2 P90, TiO_2 P25, and La_2O_3 single layers.

given by equation [55,56]:

$$(\alpha h\upsilon)^n = A\left(h\upsilon - E_g\right) \tag{4}$$

Where, E_g is the band gap energy, A is a constant, and n depends on the type of electronic transition (typically $n = 2$ for indirect transitions).

The band gap energies of TiO_2 P90, TiO_2 P25, and La_2O_3 were determined to be 3.30 eV, 3.00 eV, and 5.13 eV, respectively, as determined by Tauc plot analysis. These values signify the minimum energy required for the materials to undergo electronic transitions from the valence band to the conduction band. TiO_2 P90 and TiO_2 P25 exhibit band gap energies within the typical range for wide-bandgap semiconductors, making them suitable for applications in photocatalysis and solar cells. La_2O_3, with a higher band gap energy, may find applications in various electronic devices that require materials with wider band gaps.

In Fig. 4(b), the absorbance vs. wavelength plot provides precise information on the photo-absorption characteristics of the investigated photoanodes. Each material exhibits distinctive absorption patterns, contributing to a comprehensive understanding of its optical properties. For TiO_2 P90, the absorption spectrum reveals prominent peaks within the wavelength range of 285 nm–370 nm. This absorption region spans both the UV and visible spectra. The absorption of photons in this range indicates the capability of TiO_2 P90 to harness energy from both UV and visible light, making it useful for applications where a broad spectrum of light needs to be absorbed, such as in photocatalysis and solar energy conversion. Similarly, TiO_2 P25 displays an absorption region extending from 280 nm to 400 nm, encompassing both the UV and visible regions. The similarity in the absorption profiles of TiO_2 P90 and TiO_2 P25 suggests that both materials share comparable optical properties, with effective light absorption across a broad spectrum. This characteristic is advantageous for their utility in various photoelectrochemical and photovoltaic applications.

In contrast, La_2O_3 exhibits a narrower absorption wavelength region centered on 240 nm, primarily in the UV region. Furthermore, the observed lower absorption intensity in comparison to TiO_2 indicates that La_2O_3 is less efficient in absorbing light. The narrower absorption range and reduced absorbance in the UV region suggest that La_2O_3 may be better suited for applications where sensitivity to specific UV wavelengths is desired.

The differences in absorption characteristics among TiO_2 P90, TiO_2 P25, and La_2O_3 provide valuable insights into their suitability for different applications based on their spectral response. These findings contribute to the optimization of materials for specific functions in optoelectronic devices. They highlight the importance of tailoring materials to achieve the desired absorption properties for targeted applications.

Fig. 5 illustrates the Mott-Schottky plots for TiO_2 and La_2O_3 photoanodes measured at the frequency of 2000 Hz, referenced against Pt. These plots are crucial for analyzing the semiconductor properties of the materials. As Fig. 5(a), TiO_2 exhibits typical n-type behavior, with a linear region intercept providing us with a flat-band potential of −0.93 V (vs. Pt) at 2000 Hz. The negative flat band potential confirms that donor levels are situated near the conduction band edge, allowing electrons to accumulate under illumination, a principal requirement for efficient electron injection from the N719 dye. These results are consistent with those previously reported flat-band potential values for TiO_2 (−0.52 to −0.86 V) [57], which verify the optoelectronic characteristics of our material. Conversely, Fig. 5(b) exhibits a p-type nature for La_2O_3 with a positive flat band potential of +1.06 V. This indicates acceptor levels near the valence band edge to facilitate hole accumulation and to create an energy barrier to avoid electron back-transfer. The flat band potential measured is like literature values for La_2O_3 (+1.0 to +1.2 V) [58] and corroborates its role as a charge-separating layer. Both materials exhibit no significant frequency dependence (<0.1 V shift from 500 to 2000 Hz), indicating low surface state densities. The cleanliness of the interface directly enables enhanced charge transport in our devices, as indicated by the high J_{SC} (17.70 mA cm^{-2}), V_{OC} (0.731 V), and low R_{rec} (11.35 Ω cm^{-2}).

The frequency-dependent shift in the flat-band potentials for both TiO_2 and La_2O_3 suggests a dynamic response of the photoanodes to the applied AC signal, affecting the charge distribution and potential barriers at the electrode/electrolyte interface. These findings are critical for understanding the charge transfer processes and optimizing the performance of these materials in photoelectrochemical applications.

Fig. 6 illustrates the band diagrams of a DSSC utilizing TiO_2 (n-type) and La_2O_3 (p-type) particles as photoanodes, along with N719 dye. In this setup, the dye molecules are adsorbed onto both TiO_2 and La_2O_3 particles, enabling electron excitation and transfer from both types of particles. p-La_2O_3 serves as a blocking layer at its higher conduction band edge, effectively reducing electron-hole recombination. Additionally, the integrated p-La_2O_3 layer facilitates efficient charge separation, illustrated in Fig. 6.

Fig. 6(b) illustrates the contributions of n-TiO_2, p-La_2O_3, and the dye in the electron transfer process within the DSSC, as the dye is attached to both TiO_2 and La_2O_3 particles. Consequently, three distinct electron transfer pathways need to be considered: dye-TiO_2, dye-La_2O_3, and TiO_2-La_2O_3. These pathways are clearly depicted in Fig. 6(b). Conversely, hole transfer occurs in the opposite direction to electron transfer, as also shown in Fig. 6.

The La_2O_3 conduction band edge at 5.13 eV serves as a kinetic recombination barrier, yet it is suitable for efficient electron injection

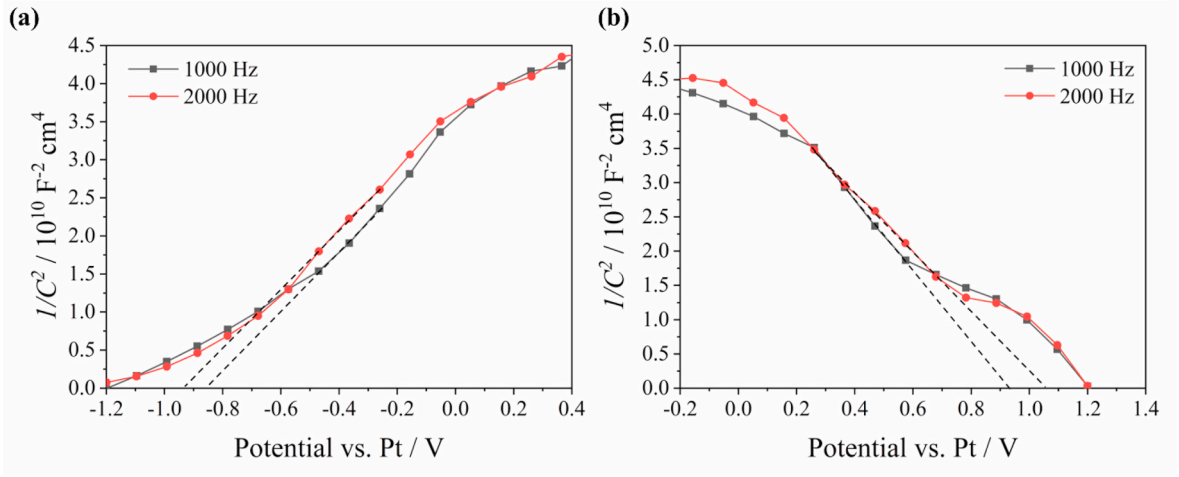

Fig. 5. Mott-Schottky plots for (a) TiO_2, (b) La_2O_3 at the frequency of 2000 Hz, referenced against Pt.

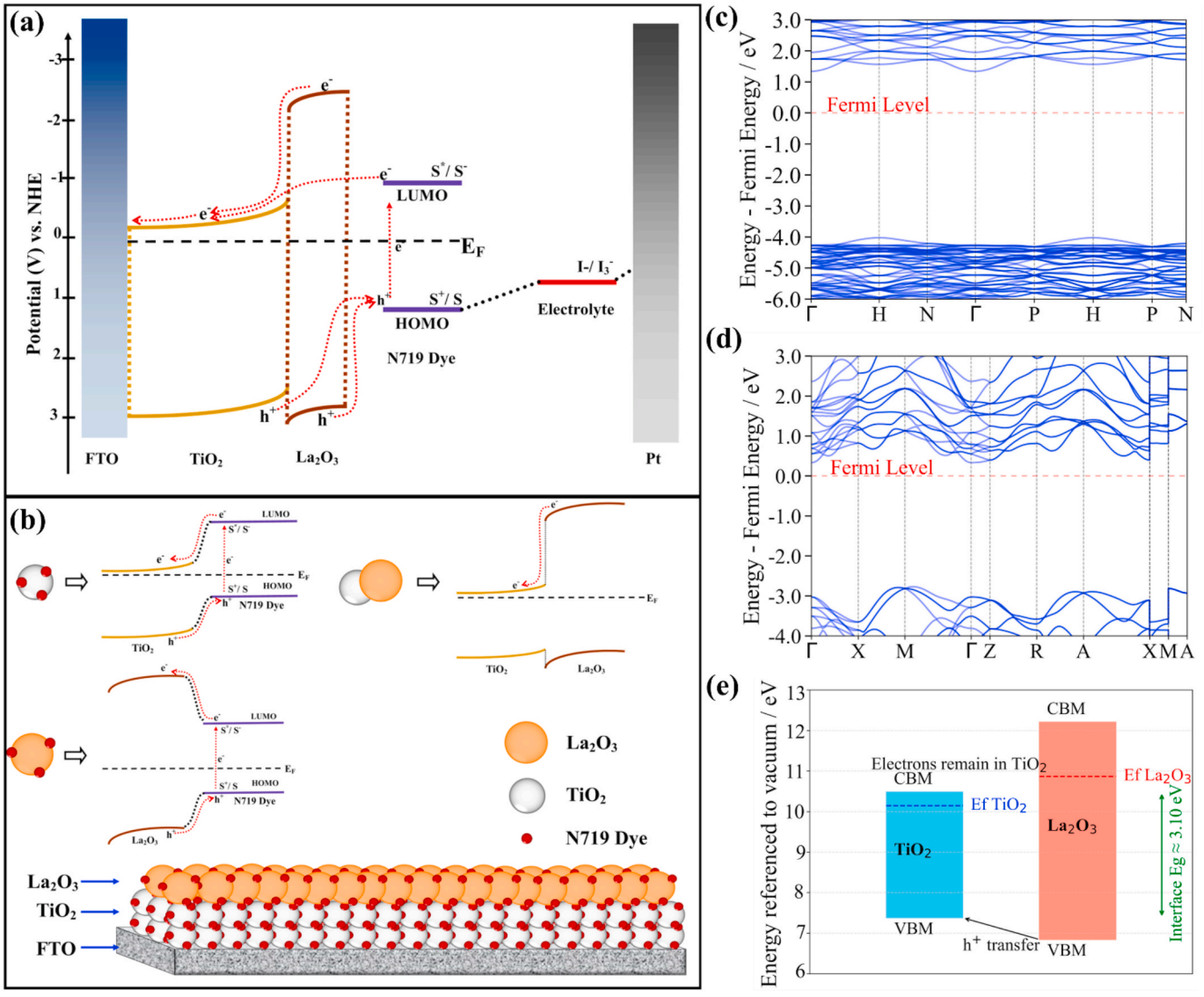

Fig. 6. Schematic band diagram (based on real values) and electron-hole transfer; (a) during the operation of the DSSC, (b) among each particle on the photoanode (La_2O_3, TiO_2, and N719 Dye), (c) DFT + U-calculated electronic band structure of La_2O_3, (d) DFT + U-calculated electronic band structure of TiO_2, and (e) DFT + U-based band alignment of the TiO_2/La_2O_3 heterostructure, referenced to the vacuum level.

from the dye. The DSSC, as illustrated in Fig. 6, utilizes both TiO_2 (n-type) and La_2O_3 (p-type) particles in the photoanode with N719 dye molecules adsorbed on both compounds. Though the LUMO (~3.5 eV) of the dye injects electrons directly into the lower conduction band edge of TiO_2 (~3.2 eV), the La_2O_3 layer's high conduction band edge presents an energy barrier to prevent back-transfer of TiO_2 electrons into the electrolyte (Fig. 6(a)). There exist three distinct channels for charge transfer in this system as discussed above (Fig. 6(b)).

The system's efficiency arises because:

(i) The dye-TiO_2 injection channel remains dominant by virtue of favorable band alignment,
(ii) Its position at the top of the TiO_2 multilayers (following deposition) allows direct dye molecule access to TiO_2,
(iii) The thin La_2O_3 layer (1.43 μm) facilitates efficient charge transport while suppressing recombination, and
(iv) p-La2O3 also facilitates hole transfer in the back direction, inducing charge separation.

This process is facilitated by the improved J_{SC} (17.70 mA cm^{-2}, Table 4) and reduced R_{rec} (11.35 Ω cm^{-2}, Table 5), indicating a simultaneous improvement in charge collection and a reduction in recombination.

Combining these transfer processes, Fig. 6(a) presents the overall electron and hole transfer mechanisms within the DSSC. This comprehensive depiction accounts for the interaction between the dye, TiO_2, and La_2O_3 particles, illustrating the complete transfer process in the operational DSSC.

3.4. DFT characterization of the photoanode

For TiO_2, applying a U value of 8.3 eV to the Ti 3d orbitals yielded a band gap of 3.10 eV, closely matching the experimental value of ~3.2 eV, indicating appropriate treatment of electron correlation. For La_2O_3, the plain GGA band gap of 3.57 eV increased to 5.36 eV when a U value of 7.0 eV was applied to the O 2p orbitals, aligning well with the expected ~5.7 eV. Bulk structures were optimized, and a slab model of TiO_2 (45 Å) and La_2O_3 (15 Å) layers were constructed with vacuum spacing to avoid periodic interactions. Bulk calculations provide a strong theoretical basis supporting experimental band alignment and charge separation.

A band alignment diagram using DFT + U results, referenced to the vacuum level, shows a type-II staggered alignment: the conduction band minimum of TiO_2 lies just below that of La_2O_3. In contrast, its valence band maximum is significantly higher. This confines photoexcited electrons to TiO_2, preventing transfer to La_2O_3, and allows holes to relax into La_2O_3's deeper valence band, promoting charge separation and reducing recombination. The Fermi level of TiO_2 sits higher than that of La_2O_3, consistent with their n-type and p-type nature. Fig. 6(c) presents the electronic band structure of La_2O_3 calculated using the DFT + U method. The results reveal a wide band gap accompanied by a deep valence band, indicative of strong p-type semiconducting behavior. Fig. 6(d) shows the DFT + U calculated electronic band structure of TiO_2, characterized by an indirect band gap. The positions of the conduction band minimum and valence band maximum further confirm the n-type nature of TiO_2. Fig. 6(e) presents the DFT + U-calculated band alignment of the TiO_2/La_2O_3 heterostructure referenced to the vacuum level. The system exhibits a type-II (staggered) band alignment, where electrons are confined within the TiO_2 conduction band while holes preferentially transfer to the La_2O_3 valence band. The predicted interface band gap is approximately 3.10 eV, determined by the lowest conduction band minimum and highest valence band maximum across the interface. This value corresponds to the bulk band gap of TiO_2, indicating that there is no significant band gap narrowing at the interface. Nonetheless, the staggered alignment enables efficient charge separation, as illustrated in Fig. 6(e).

The current bulk-level results suggest that the p-type La_2O_3 layer acts as an electron-blocking and hole-transporting barrier, enhancing charge separation at the interface. Although the interface band gap estimate does not consider interfacial states or band bending, it aligns with the experimentally observed enhanced photovoltaic performance. These findings underscore the importance of band alignment engineering in optimizing charge separation and minimizing recombination in TiO_2/La_2O_3 systems.

Table 4
Characteristic parameters for control and developed DSSCs by depositing p-La_2O_3 charge separation layer.

Photoanode type	J_{SC}/mA cm^{-2}	V_{OC}/V	*ff*	*PCE*/%
TiO_2 (6 layers)	13.4	0.71	0.66	6.34
TiO_2 (5 layers) + La_2O_3 (1 layer)	17.7	0.73	0.66	8.50

Table 5
EIS characteristic parameters of the control DSSC and one improved by integrating a p-type La_2O_3 layer into the photoanode.

Photoanode type	R_{tr}/Ω cm^{-2}	R_{rec}/Ω cm^{-2}	τ_{rec}/ms	τ_{tr}/ms	D_L/μm
TiO_2 (6 layers)	4.74	19.05	254.62	0.03	10.42
TiO_2 (5 layers) + La_2O_3 (1 layer)	2.35	11.35	59.33	0.04	12.57

3.5. Photovoltaic performances of DSSCs

This study meticulously examined the consequential impact of a p-La_2O_3 charge separation layer on the performance of DSSCs. The comparative analysis involved scrutinizing the current density versus cell potential (*J-V*) behavior and power density versus cell potential (*P-V*) behavior of two distinct configurations: the control DSSC, featuring a photoanode with n-type TiO_2 in 6 layers, and the developed DSSC, incorporating n-type TiO_2 in 5 layers with an additional layer of p-La_2O_3. Graphical representations in Fig. 7 (a) and (b) illustrate the possible mechanism for the superior performance of the developed DSSC compared to the control cell. This indicates the beneficial influence of the p-La_2O_3 charge-separating layer on the overall efficiency of the DSSC. It is essential to emphasize that, despite the absence of sealing throughout the experimentation, all investigated gel polymer electrolyte-based cells demonstrated efficiencies exceeding 6 %. This notable outcome in the quasi-solid-state configuration may be due to a confluence of factors, including the intrinsic characteristics of the multilayer photoanode, the suitability of the gel polymer electrolyte system, and the Pt counter electrode used in the study.

Remarkably, the solid-state DSSC featuring a p-La_2O_3 layer within the photoanode demonstrated higher efficiency, primarily attributed to its advantageous properties in mitigating electron recombination within the cell, thereby enhancing carrier separation. Consistent with earlier expectations and detailed explanations, the DSSC with the p-La_2O_3 charge-separating layer exhibited notably elevated values for key parameters such as J_{SC}, V_{OC}, *ff*, and PCE. This substantiates the intrinsic superiority of charge-separating layer-based DSSCs, providing compelling evidence for their merit in advancing the broader landscape of photovoltaic cell technologies. For a more detailed insight, the primary parameters, including V_{OC}, J_{SC}, *ff*, and PCE, as assessed through *J-V* measurements, are presented in Table 4, further elucidating the substantial enhancements conferred by the p-La_2O_3 charge-separating layer on the DSSC performance.

The investigation encompassed two distinct formulations to understand the discernible enhancement in efficiency observed in the DSSC incorporating the p-La_2O_3 layer, resulting in a noteworthy PCE of 8.50 %, accompanied by a corresponding J_{SC} of 17.70 mA cm^{-2}. These PCE and J_{SC} values exhibited are remarkably high values for a quasi-solid-

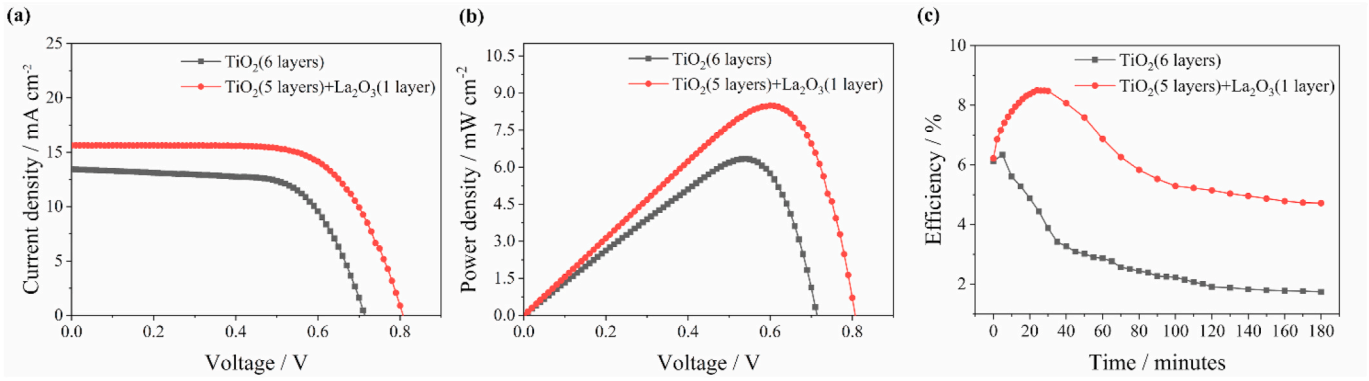

Fig. 7. (a) The current density vs. cell potential, (b) The power density vs. cell potential for control and developed DSSCs by depositing p-La_2O_3 charge separation layer, and (c) The efficiency variation over time for the unsealed control (without p-La_2O_3 layer) and developed DSSCs by integrating p-La_2O_3 charge-separating layer.

state DSSC [59,60]. Compared to the control DSSC, which employed six layers of TiO_2 for the photoanode without a blocking layer, the control DSSC exhibited a lower PCE value of 6.34 %. This discrepancy highlights the beneficial impact of the p-La_2O_3 charge-separating layer on the overall efficiency of the DSSC. Specifically, the DSSC incorporating the p-La_2O_3 blocking layer demonstrated a remarkable 34.07 % enhancement in PCE compared to the control DSSC, which utilized bare n-TiO_2 without any blocking layer. This pronounced improvement underscores the efficacy of the p-La_2O_3 charge-separating layer in augmenting the photovoltaic performance of the DSSC.

These data provide compelling evidence that the blocking layer plays a crucial role in mitigating factors that hinder efficiency, ultimately leading to a substantial increase in the photovoltaic conversion capabilities of the DSSC. The nuanced understanding of the interplay between the blocking layer and the photoanode composition contributes valuable insights to the ongoing advancement of DSSC technology.

Fig. 7 (c) provides a preliminary glimpse into the short-term stability of solar cells by monitoring their efficiencies over 3 h. The investigation reveals a noteworthy trend where the efficiencies of the control cell exhibited a gradual decrease throughout the measurement period. In stark contrast, the developed cell, incorporating the p-La_2O_3 charge-separating layer, demonstrated remarkable stability throughout the entire experiment. While this preliminary test demonstrates the positive impact of the p-La_2O_3 layer in retarding short-term degradation, long-term stability tests must be carried out to confirm the complete stability of the resulting DSSCs. The observed decline in efficiency for the control cell underscores inherent challenges related to short-term stability. However, the developed cell, featuring the blocking layer, exhibited a significantly higher level of stability and efficiency compared to its control counterpart. This disparity in stability profiles highlights the beneficial effect of the p-La_2O_3 charge-separating layer in mitigating degradation or performance deterioration over time.

3.6. *Electrochemical impedance spectra analysis of DSSCs*

The Nyquist plots, depicted in Fig. 8(a), exhibit a distinctive feature characterized by the presence of only two primary semicircles. This characteristic behavior can be linked to the relatively high conductivity exhibited by the Gel Polymer Electrolytes (GPEs) utilized in this study. The appearance of a singular semicircle is indicative of Nernstian diffusion phenomena about the I_3^- ions within these GPEs [61,62]. This manifestation suggests a facilitated and efficient ion diffusion process within the GPEs, emphasizing their favorable conductivity properties. To delve into the intricate electrochemical dynamics, a simpler equivalent circuit model, as shown in the inset of Fig. 8(a), was utilized. The utilization of an equivalent circuit enables the extraction of valuable information regarding the impedance components inherent in the DSSCs and aids in interpreting the underlying electrochemical processes.

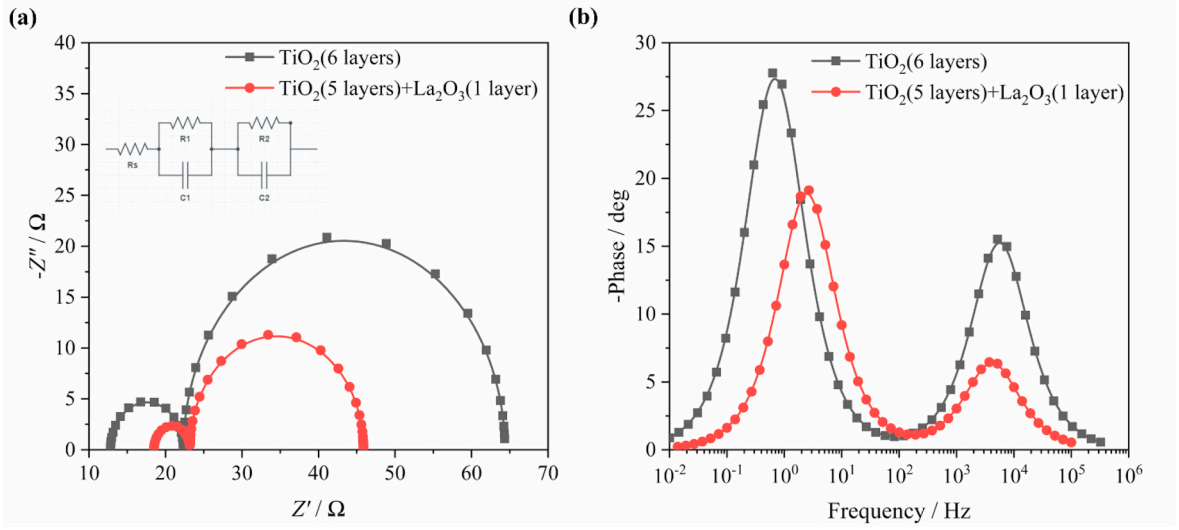

Fig. 8. (a) Nyquist, (b) Bode phase plots of the control and developed DSSCs by integrating a p-type La_2O_3 layer in the photoanode. The chi-square (χ^2) values are 0.097 for the control cell and 0.053 for the developed cell.

The corresponding parameters derived from the model are presented in Table 5. Notably, one of the key parameters, R_{tr}, reflects the impedance encompassing the charge transfer phenomena occurring at the platinum (Pt) electrode-electrolyte interface [63]. This parameter provides insights into the kinetics of charge transfer at the critical interface, shedding light on the efficiency of electrochemical reactions occurring at the Pt electrode. Conversely, another vital parameter, R_{rec}, associated with the semicircular feature observed in the mid-frequency region of the Nyquist plots, signifies the resistance to the collection and transportation of injected electrons inside the TiO_2 film. Additionally, R_{rec} encapsulates the charge transfer processes transpiring along the interfaces involving TiO_2/dye/electrolyte [64,65]. This parameter is instrumental in characterizing the efficiency of electron transport and charge transfer within the intricate DSSC architecture. In summary, the Nyquist plots, combined with the use of an equivalent circuit model and the derived parameters in Table 5, provide a detailed understanding of the complex electrochemical processes occurring within DSSCs.

To place the electrochemical performance of our Pt-based counter electrode into context, we compare our EIS data with those from the literature. R_{tr} of our device, 2.35 Ω cm^{-2} (Table 5), is much lower than that quoted by the reported values of R_{tr} of 222.7 Ω cm^{-2} for home-made carbon counter electrode [66], and the recent study [67], utilized an opaque Pt counter electrode which was deposited using a chemical bath to achieve a very much lower value of R_{tr} of 0.89 Ω cm^{-2}. These comparisons demonstrate the effectiveness of our Pt counter electrode, which ensures optimal catalytic activity and low interfacial resistance, pivotal to practical redox cycling in DSSCs.

As previously discussed, the R_{rec} value denotes the resistance associated with the development and transition of injected electrons within the porous TiO_2 film, as well as the charge transfer occurring at the interfaces of TiO_2/dye/electrolyte [64,65]. Data in Table 5 show that the developed cell under scrutiny demonstrated a remarkable reduction in its R_{rec} value, registering 11.35 Ω cm^{-2}. This notable diminution was in stark contrast to the control cell, which featured bare TiO_2, where the R_{rec} value was 19.05 Ω cm^{-2}. This discrepancy implies a substantially enhanced efficiency in terms of electron generation and transportation within the developed cell. Furthermore, the observed decrease in R_{rec} signifies a lower rate of hole-electron recombination, highlighting superior charge carrier dynamics in the developed cell when compared to its bare TiO_2 counterpart. Measured R_{rec} values correspond well with values reported in recent studies of high-performance photoanodes. For instance, the Ni-doped TiO_2/TiO_2 photoanode exhibited a higher R_{rec}, consistent with its improved charge separation efficiency compared to our device [68]. Conversely, our photoanode possesses a higher R_{rec} compared to plasmonic nanoparticle (Ag/Au)-modified counterparts reported in Ref. [69], suggesting improved charge-carrier dynamics and reduced recombination losses in our device.

To calculate the electron persistence in recombination (τ_{rec}) within the solar cell, observe the position of the low-frequency peak in the Bode phase plots, which may be represented as $\tau_n = 1/2\pi f$, where 'f' denotes the frequency of the applied AC voltage, as already specified [70]. When the solar cell operates in open-circuit mode with light, two distinct frequency peaks emerge in the EIS spectra. The low-frequency peak, which ranges from 10^{-1} to 100 Hz, corresponds to the transit of injected electrons into porous TiO_2 sheets, as well as the following charge transfer processes that occur at the TiO_2/dye/electrolyte interface. The high-frequency peak (in the kHz range) can be ascribed to charge transfer processes occurring at the interfaces of the redox pair and the platinum (Pt) electrode [71].

The investigation focused on the effect of the photoanode with a blocking layer on diffusion length as part of the study on diffusion length effects (D_L) related to electrolyte composition. The diffusion length is the distance an electron may travel across a substance before recombining with a hole. The work used impedance data analysis to determine electron diffusion lengths [72–74]. Particularly, the electron diffusion lengths were calculated using the equation:

$$D_L = L\sqrt{\frac{R_{rec}}{R_{tr}}} \quad (5)$$

Where, R_{rec} and R_{tr} denote the recombination and charge transfer resistances. L represents the thickness of the sample. In the preliminary investigation [48], the thickness of the samples was estimated by evaluating transverse scanning electron microscopy (SEM) images, and a 3D mapping image in Fig. 2 (B) was constructed to provide a method for determining the parameter. The computed values for electron diffusion length are shown in Table 5.

In this study, a higher diffusion length of 12.57 μm was observed for the cell with the p-type La_2O_3 blocking layer photoanode, which also exhibited the highest efficiency among the examined cells. This observation is consistent with recent findings in Ni-doped TiO_2/TiO_2 systems, where the highest-efficiency solar cell also demonstrated an increased diffusion length [68]. This finding means that electrons in the developed cell with an La_2O_3 layer can travel farther before being recombined. This resulted in improved overall efficiency for this particular cell.

3.7. Comparative analysis against state-of-the-art DSSCs

The performance of our quasi-solid-state DSSC based on a p-La_2O_3 charge-separating layer exhibits advancements in multiple aspects of DSSC technology. With 8.50 % PCE, our device not only outperforms phosphor-assisted DSSCs (7.16 % PCE) that leverage $SrAl_2O_4$:Eu^{2+} for light management [75] but also outcompetes fiber-shaped DSSCs with TiN nanorod counter electrodes (5.69 %) and N719/Ru(II)-bipyridine co-sensitized systems (6.3 %) [76]. While fibrous DSSCs with Ni_3Te_2 counter electrodes achieve higher PCE values (11.81 %) owing to enhanced catalytic activity [77], our approach uniquely addresses the intrinsic problem of charge recombination at the photoanode/electrolyte interface, a critical limitation in conventional designs. This 17.70 mA cm^{-2} J_{SC} far exceeds those achieved for both phosphor-modified systems (15.68 mA cm^{-2}) and fiber-shaped DSSCs with TiN nanorods, underscoring the excellent charge transport behavior achieved with our ultra-thin p-La_2O_3 blocking layer (1.43 μm). This design yields an outstanding 34.07 % PCE improvement over unmodified TiO_2, outperforming 14–14.6 % improvements achieved for Pt or CoSe-modified counter electrodes [78]. Importantly, our quasi-solid-state architecture maintains excellent stability (>80 % retention after 3 h without sealing) while avoiding the mechanical degradation problems besetting fiber-shaped DSSCs (15.3 % PCE loss after 5500 bending cycles) [73]. Compared to approaches relying on structural flexibility, panchromatic sensitization, or phosphor-based light management, our p-La_2O_3 incorporation provides a scalable and straightforward solution to interfacial charge recombination without sacrificing compatibility with traditional device designs. When compared to multilayer TiO_2-based DSSCs (as detailed in Table 6), our

Table 6
Performance comparison of different multi-layer TiO_2-based DSSCs.

Photoanode	J_{SC}/mA cm^{-2}	V_{OC}/V	*ff*	*PCE*/%	Reference
n-TiO_2/p-La_2O_3	17.70	0.73	0.66	8.50	This work
TT/TS/TiO_2-P25/post-TS	7.11	0.63	0.56	8.43	[79]
TiO_2/AZO/TiO_2	12.39	0.72	0.65	5.77	[80]
TiO_2 - 6 layers	12.10	0.71	0.62	5.30	[48]
TiO_2 - 6 layers (GPE)	17.70	0.73	0.68	8.76	[51]
TiO_2 (TDR)	15.17	0.73	0.68	7.52	[81]
Fluorine doped TiO_2	17.62	0.60	0.70	7.46	[82]
Co-doped TiO_2 - 3 layers	11.04	0.87	0.59	5.66	[83]
BTP/BTR/BTN (Brookite)	16.54	0.70	0.70	8.16	[84]
TiO_2/rGO	15.82	0.72	0.58	6.60	[85]
Hollow TiO_2 - 3 layers	16.26	0.68	0.72	8.08	[86]

p-La_2O_3 blocking layer further proves its superiority in enhancing device performance. This combined performance of high efficiency, stability, and simplicity positions our p-La_2O_3 approach as a versatile and revolutionary technique for elevating DSSC technology to new levels beyond current limitations.

4. Conclusions

The surface modification of TiO_2 photoanodes with p-La_2O_3 was shown to establish a energy barrier at the photoanode-electrolyte interface. The barrier mitigates recombination of photogenerated electrons and dye cations. The successful surface modification was confirmed by comprehensive analyses. These included SEM imaging, XRF and XRD examinations, as well as an investigation of optical properties using UV–Vis spectroscopy. SEM images provided visual evidence of the altered surface morphology. XRF and XRD analyses provided elemental and structural insights, respectively, confirming the successful integration of p-La_2O_3 into the n-TiO_2 surface. The optical properties of the modified photoanodes were systematically examined using UV–Vis spectroscopy. Specifically, the DSSCs incorporating an ultra-thin layer of p-La_2O_3 exhibited a remarkable increase in PCE from 6.34 % to 8.50 %, signifying a notable 34.07 % improvement over the cells, without surface modification. The observed enhancement highlights the effectiveness of p-La_2O_3 as a charge-separating layer, significantly contributing to improved DSSC performance. Higher short-term cell stability is a remedy for selected gel polymer electrolytes. The higher short-term cell stability is attributed to the use of a selected gel polymer electrolyte. While these results are promising, the major limitation of this study is that the particle size of La_2O_3 was relatively large (327.32 nm), which may restrict light absorption compared to smaller nanoparticles with a larger surface area. While short-term stability testing over 3 h was promising, additional prolonged testing under operating conditions would be beneficial to assess durability fully. In summary, the application of p-La_2O_3 as a surface modification layer for n-TiO_2 photoanodes resulted in a higher carrier diffusion length of 12.57 μm, indicating enhanced forward electron transport and reduced recombination losses. These findings highlight the potential of p-type La_2O_3 as an effective layer for enhancing efficiency in DSSC technology. La_2O_3 also exhibits excellent commercial potential for DSSCs, with material costs comparable to those of conventional TiO_2 and compatibility with existing spin-coating deposition processes. Demonstrated stability and straightforward integration into existing production processes will facilitate simple scale-up. Further optimization through particle size reduction may maximize both deposition yield and device performance while remaining cost-effective.

CRediT authorship contribution statement

T.M.W.J. Bandara: Writing – review & editing, Writing – original draft, Supervision, Project administration, Methodology, Investigation, Funding acquisition, Formal analysis, Conceptualization. **R.D.M.A.C.B. Rajakarunarathne:** Writing – original draft, Methodology, Investigation, Formal analysis, Conceptualization. **R.P. Chandrika:** Writing – review & editing, Visualization, Investigation, Formal analysis, Conceptualization. **L. Ajith De Silva:** Writing – review & editing, Investigation, Formal analysis, Conceptualization. **Kirthi Tennakone:** Writing – review & editing, Investigation, Data curation, Conceptualization. **G.R.A. Kumara:** Writing – review & editing, Investigation, Formal analysis, Conceptualization. **H.M.J.C. Pitawala:** Writing – review & editing, Resources, Formal analysis, Conceptualization. **Prasad S. Wanninayake:** Writing – review & editing, Investigation, Formal analysis.

Funding

Financial assistance from the Research Grant No. PGIS/2022/12, Post-graduate Institute of Science, University of Peradeniya, Sri Lanka, and University Research Council Grant No. 346, University of Peradeniya, Sri Lanka, is acknowledged.

Declaration of competing interest

The authors declare that they have no known competing financial interests or personal relationships that could have appeared to influence the work reported in this paper.

Acknowledgments

Mr. B.P. Gunawardhana, Department of Physics, Faculty of Science, University of Peradeniya, Sri Lanka, is greatly acknowledged.

Data availability

Data will be made available on request.

References

[1] L. Meng, C. Li, Blocking layer effect on dye-sensitized solar cells assembled with TiO_2 nanorods prepared by DC reactive magnetron sputtering, Nanosci. Nanotechnol. Lett. 3 (2) (2011) 181–185.
[2] L. Giribabu, Green materials for tapping solar energy, Int. J. Lumin Appl. 5 (2015) 175–177.
[3] B. O'regan, M. Grätzel, A low-cost, high-efficiency solar cell based on dye-sensitized colloidal TiO_2 films, Nature 353 (6346) (1991) 737–740.
[4] C.G. Ezema, A.C. Nwanya, B.E. Ezema, B.H. Patil, R.N. Bulakhe, P.O. Ukoha, C. D. Lokhande, M. Maaza, F.I. Ezema, Photo-electrochemical studies of chemically deposited nanocrystalline meso-porous n-type TiO 2 thin films for dye-sensitized solar cell (DSSC) using simple synthesized azo dye, Appl. Phys. A 122 (2016) 1–10.
[5] M. Asemi, M. Ghanaatshoar, The influence of magnesium oxide interfacial layer on photovoltaic properties of dye-sensitized solar cells, Appl. Phys. A 122 (2016) 1–7.
[6] S.M. Yong, N. Tsvetkov, L. Larina, B.T. Ahn, D.K. Kim, Ultrathin SnO_2 layer for efficient carrier collection in dye-sensitized solar cells, Thin Solid Films 556 (2014) 503–508.
[7] T.Y. Cho, S.G. Yoon, S.S. Sekhon, M.G. Kang, C.H. Han, The effect of a sol-gel formed TiO_2 blocking layer on the efficiency of dye-sensitized solar cells, Bull. Kor. Chem. Soc. 32 (10) (2011) 3629–3633.
[8] J.H. Kim, K.J. Lee, J.H. Roh, S.W. Song, J.H. Park, I.H. Yer, B.M. Moon, Ga-doped ZnO transparent electrodes with TiO_2 blocking layer/nanoparticles for dye-sensitized solar cells, Nanoscale Res. Lett. 7 (2012) 1–4.
[9] U. Mehmood, I.A. Hussein, K. Harrabi, M.B. Mekki, S. Ahmed, N. Tabet, Hybrid TiO_2–multiwall carbon nanotube (MWCNTs) photo-anodes for efficient dye sensitized solar cells (DSSCs), Sol. Energy Mater. Sol. Cell. 140 (2015) 174–179.
[10] J.B. Baxter, E.S. Aydil, Dye-sensitized solar cells based on semiconductor morphologies with ZnO nanowires, Sol. Energy Mater. Sol. Cell. 90 (5) (2006) 607–622.
[11] J.H. Lee, N.G. Park, Y.J. Shin, Nano-grain SnO_2 electrodes for high conversion efficiency SnO_2–DSSC, Sol. Energy Mater. Sol. Cell. 95 (1) (2011) 179–183.
[12] M.M. Rashad, A.E. Shalan, Hydrothermal synthesis of hierarchical WO_3 nanostructures for dye-sensitized solar cells, Appl. Phys. A 116 (2014) 781–788.
[13] Q. Liu, L. Wei, S. Yuan, X. Ren, Y. Zhao, Z. Wang, M. Zhang, L. Shi, D. Li, The effect of Ni $(CH_3COO)_2$ post-treatment on the charge dynamics in p-type NiO dye-sensitized solar cells, J. Mater. Sci. 50 (2015) 6668–6676.
[14] M. Asemi, M. Ghanaatshoar, Conductivity improvement of $CuCrO_2$ nanoparticles by Zn doping and their application in solid-state dye-sensitized solar cells, Ceram. Int. 42 (6) (2016) 6664–6672.
[15] J. Yan, F. Zhou, TiO_2 nanotubes: structure optimization for solar cells, J. Mater. Chem. 21 (26) (2011) 9406–9418.
[16] Q. Liu, Photovoltaic performance improvement of dye-sensitized solar cells based on Mg-doped TiO_2 thin films, Electrochim. Acta 129 (2014) 459–462.
[17] Y. Hong, J.Y. Liao, D. Cao, X. Zang, D.B. Kuang, L. Wang, H. Meier, C.Y. Su, Organic dye bearing asymmetric double donor-π-acceptor chains for dye-sensitized solar cells, J. Org. Chem. 76 (19) (2011) 8015–8021.
[18] I. Jinchu, A.B. Sharma, C.O. Sreekala, K.S. Sreelatha, K. Achuthan, RETRACTED: enhanced photovoltaic performance of the dye sensitized solar cell using natural dyes with surface modification of the photo-anode, in: Materials Science Forum, 771, Trans Tech Publications Ltd, 2014, February, pp. 159–168.
[19] J. Jasieniak, M. Califano, S.E. Watkins, Size-dependent valence and conduction band-edge energies of semiconductor nanocrystals, ACS Nano 5 (7) (2011) 5888–5902.
[20] E. Palomares, J.N. Clifford, S.A. Haque, T. Lutz, J.R. Durrant, Control of charge recombination dynamics in dye sensitized solar cells by the use of conformally deposited fl oxide blocking layers, J. Am. Chem. Soc. 125 (2) (2003) 475–482.
[21] M. Erdoğdu, A. Atilgan, Y. Erdogdu, A. Yildiz, Natural dyes extracted from Ligustrum vulgare, Juniperus sabina, and Papaver rhoeas for novel DSSC applications, Mater. Lett. 358 (2024) 135811.

[22] M.E. Yelkovan, M. Erdogdu, Y. Erdogdu, A. Yildiz, Driving forces of injection and regeneration in natural dye-sensitized solar cells: insights into photovoltaic performance, B. D. U. L. L. A. H. Sol. Energy 295 (2025) 113523.

[23] M. Erdogdu, A. Atilgan, Y. Erdogdu, A. Yildiz, Flavonoid from Hedera helix fruits: a promising new natural sensitizer for DSSCs, J. Photochem. Photobiol. Chem. 448 (2024) 115288.

[24] N. Akdogan, M. Alp, A. Atilgan, A. Disli, Y. Erdogdu, A. Yildiz, An AZO dye with nitril anchoring to dye-sensitized solar cell performance: a theoretical and experimental investigation, Mater. Lett. 351 (2023) 135075.

[25] A.R. Al-Marhabi, R.M. El-Shishtawy, K.O. Al-Footy, E. Atilgan, A. Atilgan, A. Yildiz, The impact of aryl amine donors on the performance of dye-sensitized solar cells based on quinoxaline D-π-A-π-A sensitizers, J. Mol. Struct. 1333 (2025) 141746.

[26] C. Bai, D. Fang, W. Ding, J. Wen, D. Wang, B. Mi, Z. Gao, Electrophoretically achieved thick and high-quality NiO film as photocathode for high-performance P1-Based p-DSSCs, ACS Appl. Electron. Mater. 7 (6) (2025) 2546–2556.

[27] Z. Xu, D. Xiong, H. Wang, W. Zhang, X. Zeng, L. Ming, W. Chen, X. Xu, J. Cui, M. Wang, S. Powar, U. Bach, Y.B. Cheng, Remarkable photocurrent of p-type dye-sensitized solar cell achieved by size controlled $CuGaO_2$ nanoplates, J. Mater. Chem. A 2 (9) (2014) 2968–2976.

[28] S. Powar, D. Xiong, T. Daeneke, M.T. Ma, A. Gupta, G. Lee, S. Makuta, Y. Tachibana, W. Chen, L. Spiccia, Y.B. Cheng, G. Gotz, P. Bauerle, U. Bach, Improved photovoltages for p-type dye-sensitized solar cells using $CuCrO_2$ nanoparticles, J. Phys. Chem. C 118 (30) (2014) 16375–16379.

[29] D. Xiong, W. Zhang, X. Zeng, Z. Xu, W. Chen, J. Cui, M. wang, L. Sun, Y.B. Cheng, Enhanced performance of p-type dye-sensitized solar cells based on Ultrasmall Mg-doped $CuCrO_2$ nanocrystals, ChemSusChem 6 (8) (2013) 1432–1437.

[30] A. Renaud, L. Cario, Y. Pellegrin, E. Blart, M. Boujtita, F. Odobel, S. Jobic, The first dye-sensitized solar cell with p-type LaOCuS nanoparticles as a photocathode, RSC Adv. 5 (74) (2015) 60148–60151.

[31] S. Du, P. Cheng, P. Sun, B. Wang, Y. Cai, F. Liu, J. Zheng, G. Lu, Highly efficiency p-type dye sensitized solar cells based on polygonal star-morphology Cu2O material of photocathodes, Chem. Res. Chin. Univ. 30 (4) (2014) 661–665.

[32] H.N. Alshareef, M. Quevedo-Lopez, H.C. Wen, R. Harris, P. Kirsch, P. Majhi, B. H. Lee, D.J. Jammy, D.J. Lichtenwalner, J.S. Jur, A.I. Kingon, Work function engineering using lanthanum oxide interfacial layers, Appl. Phys. Lett. 89 (23) (2006).

[33] H. Yu, B. Xue, P. Liu, J. Qiu, W. Wen, S. Zhang, H. Zhao, High-performance nanoporous TiO_2/La_2O_3 hybrid photoanode for dye-sensitized solar cells, ACS Appl. Mater. Interfaces 4 (3) (2012) 1289–1294.

[34] A.K. Chandiran, M.K. Nazeeruddin, M. Grätzel, The role of insulating oxides in blocking the charge carrier recombination in dye-sensitized solar cells, Adv. Funct. Mater. 24 (11) (2014) 1615–1623.

[35] X. Wu, L. Wang, F. Luo, B. Ma, C. Zhan, Y. Qiu, $BaCO_3$ modification of TiO_2 electrodes in quasi-solid-state dye-sensitized solar cells: performance improvement and possible mechanism, J. Phys. Chem. C 111 (22) (2007) 8075–8079.

[36] Y. Diamant, S. Chappel, S.G. Chen, O. Melamed, A. Zaban, Core–shell nanoporous electrode for dye sensitized solar cells: the effect of shell characteristics on the electronic properties of the electrode, Coord. Chem. Rev. 248 (13–14) (2004) 1271–1276.

[37] D.B. Menzies, L. Bourgeois, Y.B. Cheng, G.P. Simon, N. Brack, L. Spiccia, Characterization of nanostructured core-shell working electrodes for application in dye-sensitized solar cells, Surf. Coating. Technol. 198 (1–3) (2005) 118–122.

[38] A.M. Hussein, A.V. Iefanova, R.T. Koodali, B.A. Logue, R.V. Shende, Interconnected ZrO_2 doped ZnO/TiO_2 network photo-anode for dye-sensitized solar cells, Energy Rep. 4 (2018) 56–64.

[39] D.B. Menzies, Q. Dai, L. Bourgeois, R.A. Caruso, Y.B. Cheng, G.P. Simon, L. Spiccia, Modification of mesoporous TiO2 electrodes by surface treatment with titanium (IV), indium (III) and zirconium (IV) oxide precursors: preparation, characterization and photovoltaic performance in dye-sensitized nanocrystalline solar cells, Nanotechnology 18 (12) (2007) 125608.

[40] S. Vibavakumar, K.D. Nisha, V.S. Manikandan, J. Archana, M. Navaneethan, S. Harish, Enhanced photo conversion efficiency of Nb_2O_5/TiO_2 bilayer photo-anode for dye-sensitized solar cells, Opt. Mater. 140 (2023) 113828.

[41] H.K. Kim, Advanced polymeric matrices for gel electrolytes in quasi-solid-state dye-sensitized solar cells: recent progress and future perspective, Mater. Today Energy (2023) 101440.

[42] O. Bettucci, V. Saavedra Becerril, T.M.W.J. Bandara, M. Furlani, M. Abrahamsson, B.E. Mellander, L. Zani, Organic dye-sensitized solar cells containing alkaline iodide-based gel polymer electrolytes: influence of cation size, Phys. Chem. Chem. Phys. 20 (2) (2018) 1276–1285.

[43] P. Raut, V. Kishnani, K. Mondal, A. Gupta, S.C. Jana, A review on gel polymer electrolytes for dye-sensitized solar cells, Micromachines 13 (5) (2022) 680.

[44] T.M.W.J. Bandara, B.E. Mellander, I. Albinsson, M.A.K.L. Dissanayake, Effect of thermal history and characterization of plasticized, composite polymer electrolyte based on PEO and tetrapropylammonium iodide salt (Pr_4N^+ I^-), Solid State Ionics 180 (4–5) (2009) 362–367.

[45] M.H. Khanmirzaei, S. Ramesh, K. Ramesh, Effect of 1-Hexyl-3-methylimidazolium iodide ionic liquid on ionic conductivity and energy conversion efficiency of solid polymer electrolyte-based nano-crystalline dye-sensitized solar cells, J. Nanosci. Nanotechnol. 20 (4) (2020) 2423–2429.

[46] D. Singh, P.S. Dhapola, V. Singh, P.K. Singh, Polyvinylpyrrolidone with ammonium iodide and 1-hexyl-3-methylimidazolium iodide ionic liquid-doped solid polymer electrolyte for efficient dye sensitized solar cell, High Perform. Polym. 32 (2) (2020) 130–134.

[47] G.B.M.M.M. Nishshanke, B.D.K.K. Thilakarathna, I. Albinsson, B.E. Mellander, T. M.W.J. Bandara, Multi-layers of TiO_2 nanoparticles in the photoelectrode and binary iodides in the gel polymer electrolyte based on poly (ethylene oxide) to improve quasi solid-state dye-sensitized solar cells, J. Solid State Electrochem. 25 (2021) 707–720.

[48] T.M.W.J. Bandara, S.M.S. Gunathilake, G.B.M.M.M. Nishshanke, M.A.K. L. Dissanayake, N.B. Chaure, O.I. Olusola, B.E. Mellander, M. Furlani, I. Albinsson, Efficiency enhancement and chrono-photoelectron generation in dye-sensitized solar cells based on spin-coated TiO_2 nanoparticle multilayer photo-anodes and a ternary iodide gel polymer electrolyte, J. Mater. Sci. Mater. Electron. 34 (28) (2023) 1969.

[49] R.P. Chandrika, S.M.S. Gunathilaka, J.P. Liyanage, K. Wijayaratne, G.R.A. Kumara, N.G.A. Karunathilaka, L. Ajith DeSilva, T.M.W.J. Bandara, Effect of titanium dioxide nanofillers on the properties of gel-polymer electrolytes and power conversion efficiency of dye-sensitized solar cells, J. Solid State Electrochem. (2024) 1–20.

[50] T.M.W.J. Bandara, K.M.S.P. Bandara, H.M.N. Wickramasinghe, L.R.A.K. Bandara, N.M. Adassooriya, K. Wijayaratne, Enhancing dye-sensitized solar cell performance; optimization of quaternary counterion-based gel polymer electrolyte without changing additives or net-ion composition, J. Solid State Electrochem. (2024) 1–17, https://doi.org/10.1007/s10008-024-05993-5.

[51] T.M.W.J. Bandara, R.D.M.A.C.B. Rajakarunarathne, H.M.N. Wickramasinghe, L. A. DeSilva, R.P. Chandrika, S.N.F. Yusuf, Enhancing quasi solid-state dye-sensitized solar cell performance using mixed-polymer gel electrolytes: the influence of low and high molar weight polymers, J. Appl. Electrochem. (2024) 1–20.

[52] A.V. Murugan, S.C. Navale, V. Ravi, Synthesis of nanocrystalline La_2O_3 powder at 100 C, Mater. Lett. 60 (6) (2006) 848–849.

[53] T. Serin, A. Atilgan, I. Kara, A. Yildiz, Electron transport in Al-Cu co-doped ZnO thin films, J. Appl. Phys. 121 (9) (2017).

[54] A. Yildiz, H. Cansizoglu, R. Abdulrahman, T. Karabacak, Effect of grain size and strain on the bandgap of glancing angle deposited AZO nanostructures, J. Mater. Sci. Mater. Electron. 26 (8) (2015) 5952–5957.

[55] Ł. Haryński, A. Olejnik, K. Grochowska, K. Siuzdak, A facile method for Tauc exponent and corresponding electronic transitions determination in semiconductors directly from UV–Vis spectroscopy data, Opt. Mater. 127 (2022) 112205.

[56] P. Makuła, M. Pacia, W. Macyk, How to correctly determine the band gap energy of modified semiconductor photocatalysts based on UV–Vis spectra, J. Phys. Chem. Lett. 9 (23) (2018) 6814–6817.

[57] S.F. Lee, E. Jimenez-Relinque, I. Martinez, M. Castellote, Effects of Mott–Schottky frequency selection and other controlling factors on flat-band potential and band-edge position determination of TiO_2, Catalysts 13 (6) (2023) 1000.

[58] W. Ismail, A. Belal, W. Abdo, A. El-Shaer, Investigating the physical and electrical properties of La_2O_3 via annealing of $La(OH)_3$, Sci. Rep. 14 (1) (2024) 7716.

[59] N. Wang, J. Hu, L. Gao, T. Ma, Current progress in solid-state electrolytes for dye-sensitized solar cells: a mini-review, J. Electron. Mater. 49 (12) (2020) 7085–7097.

[60] S. Mahalingam, A. Nugroho, D. Floresyona, K.S. Lau, A. Manap, C.H. Chia, N. Afandi, Bio and non-bio materials-based quasi-solid state electrolytes in DSSC: a review, Int. J. Energy Res. 46 (5) (2022) 5399–5422.

[61] A.M. Zulkifli, N.I.A.M. Said, S. Bakr Aziz, E.M.A. Dannoun, S. Hisham, S. Shah, A. A. Bakar, Z.H. Zainal, H.A. Tajuddin, J.M. Hadi, M.A. Brza, S.R. Saeed, P.O. Amin, Characteristics of dye-sensitized solar cell assembled from modified chitosan-based gel polymer electrolytes incorporated with potassium iodide, Molecules 25 (18) (2020) 4115.

[62] N.M. Saidi, F.S. Omar, A. Numan, D.C. Apperley, M.M. Algaradah, R. Kasi, A. J. Avestro, R.T. Subramaniam, Enhancing the efficiency of a dye-sensitized solar cell based on a metal oxide nanocomposite gel polymer electrolyte, ACS Appl. Mater. Interfaces 11 (33) (2019) 30185–30196.

[63] A. Hauch, A. Georg, Diffusion in the electrolyte and charge-transfer reaction at the platinum electrode in dye-sensitized solar cells, Electrochim. Acta 46 (22) (2001) 3457–3466.

[64] V. Sundararajan, N.M. Saidi, S. Ramesh, K. Ramesh, G. Selvaraj, C.D. Wilfred, Quasi solid-state dye-sensitized solar cell with P (MMA-co-MAA)-based polymer electrolytes, J. Solid State Electrochem. 23 (2019) 1179–1189.

[65] U. Mehmood, H.Z. Aslam, F.A. Al-Sulaiman, A. Al-Ahmed, S. Ahmed, M.I. Malik, M. Younas, Electrochemical impedance spectroscopy and photovoltaic analyses of dye-sensitized solar cells based on carbon/TiO2 composite counter electrode, J. Electrochem. Soc. 163 (5) (2016) H339.

[66] C. Altinkaya, A. Atli, A. Atilgan, K. Salimi, A. Yildiz, Facile fabrication of low-cost low-temperature carbon-based counter electrode with an outstanding fill factor of 73% for dye-sensitized solar cells, Int. J. Energy Res. 44 (4) (2020) 3160–3170.

[67] A. Atli, A. Yildiz, Opaque Pt counter electrodes for dye-sensitized solar cells, Int. J. Energy Res. 46 (5) (2022) 6543–6552.

[68] A. Atilgan, A. Yildiz, Ni-doped TiO_2/TiO_2 homojunction photoanodes for efficient dye-sensitized solar cells, Int. J. Energy Res. 46 (10) (2022) 14558–14569.

[69] K. Salimi, A. Atilgan, M.Y. Aydin, H. Yildirim, N. Celebi, A. Yildiz, Plasmonic mesoporous core-shell Ag-Au@ TiO_2 photoanodes for efficient light harvesting in dye sensitized solar cells, Sol. Energy 193 (2019) 820–827.

[70] J. Bisquert, A. Zaban, M. Greenshtein, I. Mora-Seró, Determination of rate constants for charge transfer and the distribution of semiconductor and electrolyte electronic energy levels in dye-sensitized solar cells by open-circuit photovoltage decay method, J. Am. Chem. Soc. 126 (41) (2004) 13550–13559.

[71] J.H. Ri, J. Jin, J. Xu, T. Peng, K.I. Ryu, Preparation of iodine-free ionic liquid gel electrolyte using polyethylene oxide (PEO)-polyethylene glycol (PEG) and its application in ti-foil-based dye-sensitized solar cells, Electrochim. Acta 201 (2016) 251–259.

[72] C.W. Kuo, C.W. Huang, B.K. Chen, W.B. Li, P.R. Chen, T.H. Ho, C.G. Tseng, T. Y. Wu, Enhanced ionic conductivity in PAN–PEGME-$LiClO_4$-PC composite polymer electrolytes, Int. J. Electrochem. Sci. 8 (3) (2013) 3834–3850.
[73] D. Golodnitsky, E. Strauss, E. Peled, S. Greenbaum, On order and disorder in polymer electrolytes, J. Electrochem. Soc. 162 (14) (2015) A2551.
[74] N. Shukla, A.K. Thakur, A. Shukla, D.T. Marx, Ion conduction mechanism in solid polymer electrolyte: an applicability of almond-west formalism, Int. J. Electrochem. Sci. 9 (12) (2014) 7644–7659.
[75] E.Z. Chen, X.Y. Gu, K. Wei, Y. Cheng, Z.L. Chen, J.R. Tan, G.Z. Sun, X.J. Pan, J. Y. Zhou, E.Q. Xie, Role of long persistence phosphors on their enhancement in performances of photoelectric devices: in case of dye-sensitized solar cells, Appl. Surf. Sci. 507 (2020) 145098.
[76] J. Di Cheng, C.X. He, D. Chen, X.Y. Gu, S.K. Wang, X.P. Gao, G.Z. Sun, Z.X. Zhang, X.J. Pan, X.B. Pan, J.Y. Zhou, Effect of ruthenium (II)-bipyridine complex photosensitizer on the panchromatic light absorption and electron transfer in N719-dye sensitized photoanodes, Opt. Mater. 133 (2022) 112924.
[77] X.Y. Gu, C.Y. Zhang, J. Di Cheng, S.Q. Kang, K. Wei, G.Z. Sun, X.P. Gao, X.J. Pan, J. Y. Zhou, Tunable hierarchical hexagonal nickel telluride (Ni_3Te_2) laminated microsheets as flexible counter electrodes for high-performance fibrous dye-sensitized solar cells: accelerated electrocatalysis reduction of I_3^- ions, Chem. Eng. J. 442 (2022) 136286.
[78] X.Y. Gu, E.Z. Chen, K. Wei, L.L. Chen, C.Y. Zhang, G.W. Sun, J.R. Tan, H.S. Bi, H. Xie, G.Z. Sun, X.G.X.J. Pan, J.Y. Zhou, Design of highly ordered hierarchical catalytic nanostructures as high-flexibility counter electrodes for fiber-shaped dye-sensitized solar cells, Appl. Phys. Lett. 118 (5) (2021).
[79] A. Atli, A. Atilgan, A. Yildiz, Multi-layered TiO_2 photoanodes from different precursors of nanocrystals for dye-sensitized solar cells, Sol. Energy 173 (2018) 752–758.
[80] K. Ozel, A. Atilgan, A. Yildiz, Multi-layered blocking layers for dye sensitized solar cells, J. Photochem. Photobiol. Chem. 448 (2024) 115297.
[81] W. Wang, H. Yuan, J. Xie, D. Xu, X. Chen, Y. He, T. Zhang, Z. Chen, Y. Zhang, H. Shen, Enhanced efficiency of large-area dye-sensitized solar cells by light-scattering effect using multilayer TiO_2 photoanodes, Mater. Res. Bull. 100 (2018) 434–439.
[82] K. Subalakshmi, J. Senthilselvan, Effect of fluorine-doped TiO_2 photoanode on electron transport, recombination dynamics and improved DSSC efficiency, Sol. Energy 171 (2018) 914–928.
[83] M.I. Khan, Synthesis, characterization and application of Co doped TiO_2 multilayer thin films, Results Phys. 9 (2018) 359–363.
[84] T. Peng, J. Xu, R. Chen, A novel multilayer brookite TiO2 electrode for improved performance of pure brookite-based dye sensitized solar cells, Chem. Phys. Lett. 738 (2020) 136902.
[85] F.W. Low, C.W. Lai, N. Asim, M. Akhtaruzzaman, M. Alghoul, S.K. Tiong, N. Amin, An investigation on titanium doping in reduced graphene oxide by RF magnetron sputtering for dye-sensitized solar cells, Sol. Energy 188 (2019) 10–18.
[86] R.K. Chava, Y.T. Yu, M. Kang, Layer-by-layer deposition of hollow TiO2 spheres with enhanced photoelectric conversion efficiency for dye-sensitized solar cell applications, Nanomaterials 14 (22) (2024) 1782.